HHS Public Access

Author manuscript

Cell Rep. Author manuscript; available in PMC 2023 December 18.

Published in final edited form as:

Cell Rep. 2023 November 28; 42(11): 113378. doi:10.1016/j.celrep.2023.113378.

Data-driven multiscale model of macaque auditory thalamocortical circuits reproduces *in vivo* dynamics

Salvador Dura-Bernal[1,2,6,7,*], **Erica Y. Griffith**[1,2,6,*], **Annamaria Barczak**[2], **Monica N. O'Connell**[2], **Tammy McGinnis**[2], **Joao V.S. Moreira**[1], **Charles E. Schroeder**[2,4], **William W. Lytton**[1,5], **Peter Lakatos**[2,3], **Samuel A. Neymotin**[2,3,*]

[1]Department of Physiology and Pharmacology, State University of New York (SUNY) Downstate Health Sciences University, Brooklyn, NY, USA

[2]Center for Biomedical Imaging and Neuromodulation, Nathan S. Kline Institute for Psychiatric Research, Orangeburg, NY, USA

[3]Department Psychiatry, NYU Grossman School of Medicine, New York, NY, USA

[4]Departments of Psychiatry and Neurology, Columbia University Medical Center, New York, NY, USA

[5]Kings County Hospital Center, Brooklyn, NY, USA

[6]These authors contributed equally

[7]Lead contact

SUMMARY

We developed a detailed model of macaque auditory thalamocortical circuits, including primary auditory cortex (A1), medial geniculate body (MGB), and thalamic reticular nucleus, utilizing the NEURON simulator and NetPyNE tool. The A1 model simulates a cortical column with over 12,000 neurons and 25 million synapses, incorporating data on cell-type-specific neuron densities, morphology, and connectivity across six cortical layers. It is reciprocally connected to the MGB thalamus, which includes interneurons and core and matrix-layer-specific projections to A1. The model simulates multiscale measures, including physiological firing rates, local field potentials (LFPs), current source densities (CSDs), and electroencephalography (EEG) signals. Laminar CSD patterns, during spontaneous activity and in response to broadband noise stimulus trains,

[*]Correspondence: salvador.dura-bernal@nki.rfmh.org (S.D.-B.), erica.griffith@nki.rfmh.org (E.Y.G.), samuel.neymotin@nki.rfmh.org (S.A.N.).

AUTHOR CONTRIBUTIONS

Conceptualization, S.D.-B., E.Y.G., A.B., M.N.O., C.E.S., W.W.L., P.L., and S.A.N.; methodology, S.D.-B., E.Y.G., A.B., M.N.O., T.M., J.V.S.M., C.E.S., W.W.L., P.L., and S.A.N.; software, S.D.-B., E.Y.G., A.B., M.N.O., J.V.S.M., W.W.L., P.L., and S.A.N.; formal analysis, S.D.-B., E.Y.G., A.B., M.N.O., J.V.S.M., P.L., and S.A.N.; validation, S.D.-B., E.Y.G., and S.A.N.; investigation, S.D.-B., E.Y.G., A.B., M.N.O., T.M., P.L., and S.A.N.; data curation, S.D.-B., E.Y.G., A.B., M.N.O., P.L., and S.A.N.; writing – original draft, S.D.-B., E.Y.G., and S.A.N.; writing – review & editing, S.D.-B., E.Y.G., A.B., M.N.O., T.M., J.V.S.M., C.E.S., W.W.L., P.L., and S.A.N.; visualization, S.D.-B., E.Y.G., J.V.S.M., and S.A.N.; funding acquisition, S.D.-B., M.N.O., C.E.S., W.W.L., P.L., and S.A.N.

DECLARATION OF INTERESTS

The authors declare no competing interests.

SUPPLEMENTAL INFORMATION

Supplemental information can be found online at https://doi.org/10.1016/j.celrep.2023.113378.

mirror experimental findings. Physiological oscillations emerge spontaneously across frequency bands comparable to those recorded *in vivo*. We elucidate population-specific contributions to observed oscillation events and relate them to firing and presynaptic input patterns. The model offers a quantitative theoretical framework to integrate and interpret experimental data and predict its underlying cellular and circuit mechanisms.

In brief

Dura-Bernal, Griffith, et al. developed a realistic computational model of macaque auditory thalamocortical circuits constrained by experimental data. Their model generates realistic physiological signals across scales, including voltages, spikes, LFP/CSD, and EEG. It reproduces *in vivo* spontaneous LFP/CSD oscillation events across frequencies and predicts their underlying cellular and circuit origins.

Graphical abstract

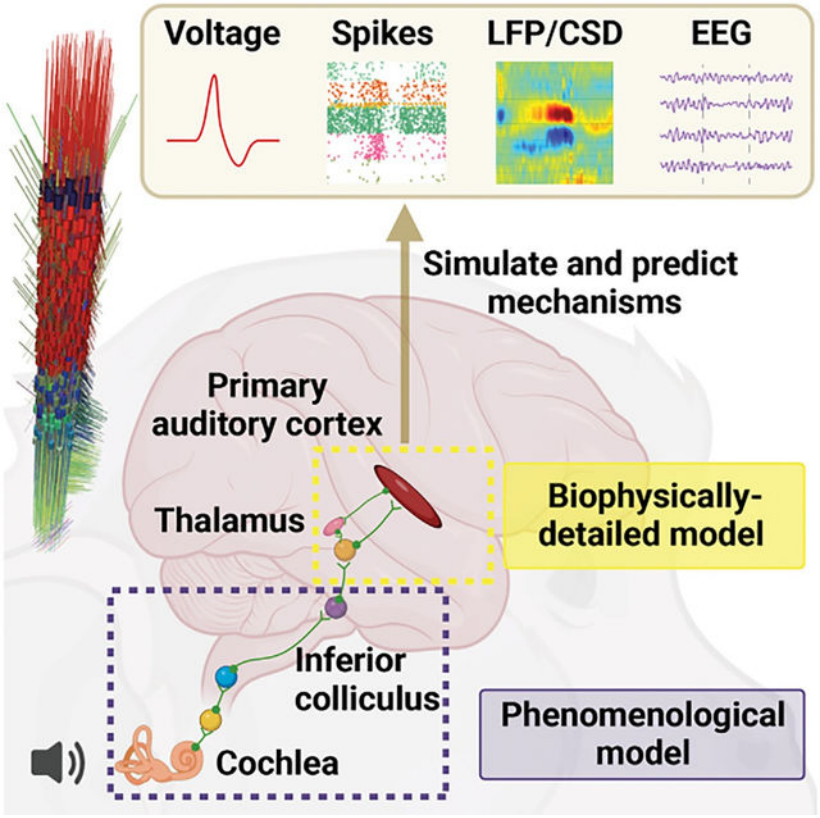

INTRODUCTION

The auditory system is involved in a number of crucial sensory functions, including speech processing,[1–4] sound localization,[5–7] pitch discrimination,[8–11] and voice recognition.[12,13] Aberrations along this pathway can result in a wide variety of pathologies. Hearing loss, for example, can result from lesions in either the peripheral[14,15] or central[16–18] parts of this

pathway, while other abnormalities can result in increased sensitivity to sound volume[19] or difficulty processing music.[20,21]

Achieving a full understanding of this system is complicated by the many interareal pathways, the complexity of the inter- and intralaminar circuitry, the heterogeneity of neuronal cell types and behaviors, and the diversity of network coding mechanisms. A growing body of experimental data, with findings drawn from different methods at different biological scales, begets the need for a framework which can integrate these disparate findings and be used to investigate the system as a whole. A framework integrating the available multiscale data would also enable us to generate predictions about the mechanisms governing oscillatory dynamics in auditory cortex, which are known to play a prominent role in neural information processing. In auditory cortex, these oscillations may be particularly important for speech processing,[22–25] with oscillations in different frequency bands synchronizing to and tracking the dynamic properties of speech waveforms.[24] In some cases, oscillatory behavior in the auditory cortex can even be used to predict speech intelligibility.[22,25] Abnormalities in auditory cortex oscillations have been observed in pathologies that include auditory processing deficits, such as schizophrenia[26–28] and autism spectrum disorder.[29,30] Increased oscillatory activity at rest,[26] strong cross-frequency synchronization,[27,28] and impaired phase locking between auditory cortex oscillations and incoming speech stimuli[29–31] have been observed in these disorders, and may help explain some of the auditory-processing-related deficits seen in these disease states.[27,29,32–34]

To address these questions, we have developed a computational model of the auditory system that integrates multiscale information on macaque cortical and thalamic circuits comprising a diversity of excitatory and inhibitory cell types with data-driven electrophysiology,[35] population densities, distribution and connectivity, including the full thalamocortical loop,[36] and realistic inputs from upstream structures such as cochlea and inferior colliculus. Bridging these hierarchical levels allows us to gain insights into the biophysical mechanisms underlying *in vivo* spontaneous activity and stimulus-evoked responses observed during experimental recordings that occur at different scales, including single-cell recordings, multiunit activity, local field potentials (LFPs), current source density (CSD), and electroencephalography (EEG). In this initial study, we simulated these multiscale recordings and validated several of them against *in vivo* macaque experimental data. We also illustrate how our model can also be used to investigate the cellular- and network-level mechanisms underlying thalamocortical oscillations in auditory cortex. This involves first reproducing similar oscillations *in silico* and then examining the activity underlying these oscillations at different scales, from subthreshold currents and dendritic effects to circuit activity in different thalamic pathways (e.g., core vs. matrix) or cortical subcircuits (e.g., pyramidal neuron-interneuron interactions). To further these types of investigations, we have made our model available to the public as a community resource for research. This also enables the community to work collaboratively and to update and extend our model as new data become available.

RESULTS

Development of a data-driven model of macaque auditory thalamocortical circuits

We developed a biophysically detailed model of macaque auditory thalamocortical circuits, including medial geniculate body (MGB), thalamic reticular nucleus (TRN), and primary auditory cortex (A1). To provide input to the thalamic populations, we connected a phenomenological model of the cochlear nucleus, auditory nerve, and inferior colliculus (IC). This resulted in a realistic model capable of processing arbitrary input sounds along the main stages of the macaque auditory pathway (Figure 1A). While details of each stage can be found in STAR Methods, the current section includes an overall description of the main features of the model.

We reconstructed a cylindrical volume of 200-μm radius and 2,000-μm depth A1 tissue (Figure 1B). The model included 12,187 neurons and over 25 million synapses, corresponding to the full neuronal density of the volume modeled. The model was divided into seven layers—L1, L2, L3, L4, L5A, L5B, and L6—each with boundaries, neuronal densities, and distribution of cell types derived from experimental data.[37–46] We included the four main classes of excitatory neurons: intratelencephalic (IT), present in all layers except L1; spiny stellate (ITS) in L4, pyramidal tract (PT) in L5B, and corticothalamic (CT) in L5A, L5B, and L6. The dendritic length of cell types in different layers was adapted according to experimental data. While many previous cortical models only include one or two interneuron types, we incorporated a greater diversity of cell type by including four classes of interneurons: somatostatin (SOM), parvalbumin (PV), vasoactive intestinal peptide (VIP), and neurogliaform (NGF). All four classes were present in all layers except L1, which only included NGF. The MGB included two types of thalamocortical neurons and thalamic interneurons. The TRN included a population of inhibitory cells. Thalamic populations were in turn divided into core and matrix subpopulations, each with distinct wiring. The total number of thalamic neurons was 721, with cell densities and ratios of the different cell types derived from published studies.

Connectivity in the model was established for each pair of the 42 cortical and thalamic populations, resulting in layer- and cell-type-specific projections (Figure 2). Each projection between populations was characterized by a probability of connection and unitary connection strength (in mV), defined as the postsynaptic potential (PSP) amplitude in a postsynaptic neuron in response to a single presynaptic spike. The probability of connection from cortical inhibitory populations decayed exponentially with cell-to-cell distance. Synapses were distributed along specific regions of the somatodendritic tree for each projection. Excitatory synapses included colocalized AMPA and NMDA receptors, and inhibitory synapses included different combinations of slow $GABA_A$, fast $GABA_A$, and $GABA_B$ receptors, depending on cell types. The values for all the connectivity parameters were derived from over 30 published experimental studies (see STAR Methods). Where available, we used data from the non-human primate auditory system, but otherwise resorted to data from other species, including rodent, cat, and human.

Afferent projections from other brain regions were modeled by providing background independent Poisson spiking inputs to apical excitatory and basal inhibitory synapses,

adjusted for each cell type to result in low spontaneous firing rates (~1 Hz). We employed automated parameter optimization methods to fine-tune the connectivity strengths to obtain physiologically constrained firing rates across all populations. It is not surprising that the initial model required some fine-tuning, given that parameters do not come from a unique individual but instead result from averaging data across animals. Additionally, some parameters were derived from data from different cortical regions and animal species. The rationale for parameter optimization was therefore to adapt synaptic strengths within biological ranges to obtain a network configuration that exhibits physiological spontaneous responses. The parameters being optimized included high-level connectivity hyperparameters, such as scaling factors for different subsets of synaptic weights grouped by synaptic type and postsynaptic layer/cell type (e.g., all inhibitory connections targeting L5 excitatory cells). As in biological systems,[47] parameter degeneracy was a feature of our model, meaning different parameter combinations could produce very similar network output. The optimization algorithm attempted to minimize an objective function, which, in short, measured the difference between the simulated and target spontaneous average firing rate for each population. Achieving a solution where all 43 populations fired within experimental ranges was particularly challenging due to the high interdependence of these populations. As a result, it was common to find solutions where one or more populations were either silent or fired at excessively high rates. We also emphasize that the parameter optimization process did not include any oscillation features or LFPs. The comparison of simulated LFP oscillatory patterns against *in vivo* experimental data was used exclusively to validate model predictions after the model had been built and optimized, based on spontaneous firing rates.

To achieve variability in the baseline model, we modified the randomization seeds used to generate the probabilistic connections and spike times of Poisson background inputs. Specifically, we ran 25 simulations with different seeds (5 connectivity × 5 input seeds), each for 11.5-s simulations (the first 1.0–1.5 s were required to reach steady state). This resulted in 250 s of simulated data, which is comparable to some of the macaque experimental datasets used. Modeling results that include statistics were calculated across all of the 25 × 10-s simulations, which provided a measure of the robustness of the model to variations in connectivity and inputs and is comparable to the variability across different macaques and trials, respectively.

We developed the models using NetPyNE[48] and parallel NEURON.[49] Overall, we ran over 500,000 simulations in order to tune the model parameters and explore model responses to different inputs and conditions. This required over 5 million core hours on several supercomputers, primarily Google Cloud Platform and the EBRAINS ICEI Fenix Infrastructure.

All model source code, results, and comparisons to experimental data are publicly available on ModelDB and GitHub: https://github.com/NathanKlineInstitute/Macaque_auditory_thalamocortical_model_data. The GitHub repository includes a detailed installation guide and system requirements, instructions for using the model and reproducing the figures, and a simplified demo of the model that can be simulated on desktop computers.

Cell-type- and layer-specific activity recorded at multiple scales

The model generated layer- and cell-type-specific spontaneous activity (Figure 3). Distinct spiking patterns were recorded across thalamus and cortex (Figure 3A): Thalamus, cortex, and TRN showed clear alpha oscillations (~8 Hz); cortical granular and supragranular layers exhibited a similar oscillatory pattern but more diffuse over time and with higher variability in peak amplitudes; and infragranular layers showed more tonic firing and a slower delta (~2 Hz) oscillation. Spiking responses also varied across cell types within a layer, e.g., L5B IT cells fired tonically whereas L5B CT cells showed phasic firing at delta frequency (only two peaks of activity). Overall, average spontaneous firing rates were below 5 Hz for excitatory neurons and below 20 Hz for inhibitory neurons, consistent with experimental data.[50–53] Spontaneous activity was simulated by driving the thalamic and cortical neurons with non-rhythmic Poisson-distributed low-amplitude background inputs. Therefore, the distinct responses of neural populations must be a consequence of their heterogeneous biophysical properties and synaptic connectivity.

The model responses were recorded and analyzed at multiple scales (Figure 3): neuronal membrane voltage traces (Figure 3C), spike times (Figure 3A), firing rate statistics (Figure 3B), LFPs and CSD analysis (Figure 3D), and current dipole moments and EEG signals (Figure 3E). These measurements represent the same underlying biophysical phenomenon as evidenced by activity features shared across them, e.g., activity peaks around 1,300 ms and 1,800 ms (see Figures 3A, 3D, and 3E). This illustrates how the model can be used to interpret common experimental measurements (multiunit activity, LFP, EEG) and relate them to the underlying biophysical circuit properties. In the final section of our results, we use this approach to disentangle the layer- and cell-type-specific biophysical sources of an oscillation event.

At each simulated electrode, the LFP was calculated based on the transmembrane currents generated at each neuronal segment and the distance between the segment and the electrode. More specifically, we used the line-source approximation method and assumed that the model neurons were immersed in an ohmic medium with a fixed conductivity of $\sigma = 0.3$ mS/mm.[54,55] Electrodes were spatially distributed at 100-μm intervals along a vertical axis of the 2,000-μm A1 column. CSD was calculated as the second spatial derivative of the LFP signal. Current dipole moments for each cell were calculated based on the transmembrane currents of each cell segment and the segment location. EEG signals were computed using forward modeling from the current dipole moments and a finite-element volume conduction model of the human head.[54,56,57] See STAR Methods for further details on the calculation of LFP and EEG signals.

Model simulations qualitatively reproduced characteristic spontaneous *in vivo* laminar LFP/CSD activity patterns recorded in macaques (Figure 4A). For instance, we observed examples in both experiment and model displaying: (1) ~50-ms-long current sinks (red) in the granular layer with current sources (blue) immediately below, plus current sources (blue) in the most superficial electrodes (Figure 4A, top); (2) ~150-ms-long current sinks fluctuating around the border of the granular and infragranular layers with current sources immediately below, and again in the most superficial electrodes (Figure 4A, middle); and (3) ~150-mslong current sources in the granular layer with current sinks above and below

(Figure 4A, bottom). While the three LFP/CSD examples share similarities, they also underscore the variability observed both within and between experimental and modeling data. In “emergence of spontaneous physiological oscillations across frequency bands,” we further quantify this variability, focusing on the oscillatory power of spontaneous responses. For reference, we also provide the associated spiking activity of all cortical and thalamic neurons during these LFP/CSD examples. It is important to note that since LFP/CSD patterns arise primarily from synaptic transmembrane currents along the dendritic tree and soma,[58,59] they do not necessarily correlate with laminar spiking activity. In “unraveling the biophysical mechanisms underlying physiological oscillations at the cellular and circuit scales,” we analyze in more depth a specific LFP/CSD oscillatory pattern and how it relates to the network spiking activity and synaptic inputs.

Next, we evaluated the responses elicited in our model by a train of short-duration broadband noise (BBN) stimuli (Figures 4B–4D). BBN results from combining a wide range of sound frequencies with equal intensity across the spectrum, providing a more ecologically valid sound than click trains. However, the short duration and regular repetition of our stimuli bear a resemblance to the temporal properties of click trains. Specifically, we generated a train of 100-msduration BBN stimuli with an interval between stimulus, or stimulus onset asynchrony, of 850 ms. Our choice of stimuli was also influenced by the availability of macaque recordings using similar BBN train stimuli, allowing direct comparison. We underscore that our model was not specifically tuned to reproduce responses to the BBN train stimulus. Nevertheless, preliminary model results capture properties of macaque *in vivo* responses to BBN, although a systematic validation remains pending.

We illustrate the full network spiking response during two consecutive BBN stimuli and quantify the IC and excitatory thalamic and cortical responses through a poststimulus time histogram (Figure 4B). IC exhibited an initial population peak response of 107 spikes/bin (coincidentally equal to 107 spikes/s/neuron, since IC has 200 neurons), which decreased to 20 spikes/bin at the end of the stimulus. Given that the BBN stimulus amplitude and spectrum are approximately flat, this marked decrease in IC spiking activity indicates an adaptation response, implemented by the auditory nerve and IC phenomenological model.[60] We note that IC responses were identical across BBN stimuli, since the phenomenological model did not include random variability. Both the thalamic and cortical excitatory populations exhibited increased peak responses when comparing a 200-ms window post- vs. prestimulus (mean ± SD peak post-pre response: thalamus = 16.8 ± 3.8 spikes/bin, $p = 0.0001$; cortex = 15.8 ± 41.4 spikes/bin, $p = 0.002$; $N = 11$, rank-sum test). Thalamic and cortical responses exhibited notable variability in response amplitude and delays, possibly influenced by the ongoing neural oscillations. Increasing the stimulus intensity may reduce the response variability. Thalamic and cortical responses did not exhibit adaptation to the repetitive BBN stimuli, potentially due to the lack of plasticity mechanisms.

Next, we compared the model average BBN CSD event-related potential (ERP) 300-ms responses against macaque *in vivo* data. Model ERP spatiotemporal patterns were consistent with experimental recordings within the supragranular, granular, and infragranular layers (Figure 4C). Finally, we illustrate an example 200-ms LFP/CSD model response evoked

by BBN stimulus exhibiting a CSD sink and source pattern similar to that recorded experimentally (Figure 4D). More specifically, both showed a ~150-ms-long current sink in the granular layer with current sources in the supragranular and infragranular layers immediately above and below. For context, we also include the corresponding model spiking raster plot including the activity of all IC, thalamic, and cortical neurons.

While reproducing responses to specific speech utterances is outside the scope of this paper, in Figure S4 we illustrate how our model transforms complex speech stimuli along the auditory pathway, from the cochlea and IC phenomenological to the biophysical thalamic and cortical model responses. We also identified examples of cortical laminar LFP/CSD patterns generated by the model that were comparable to those recorded experimentally, for example, ~150- to 200-ms-long current sinks in the granular layer, with alternating current sources and sinks in the infragranular layers (Figure S4B). However, these are isolated examples, and the model has not yet been tuned or systematically validated to reproduce the complex responses evoked by speech inputs.

Emergence of spontaneous physiological oscillations across frequency bands

Physiological oscillations across a range of frequency bands were observed in both the macaque and model thalamocortical circuits. In the model, these oscillations emerged despite having no oscillatory background inputs, suggesting they resulted from the intrinsic cellular biophysics and circuit connectivity. We quantified the power spectral density (PSD) of 10-s LFPs recorded from different macaques and from the model (Figure 5A). These results illustrate the high variability of spontaneous responses measured within and across macaques. This variability was comparable to that generated by the model. Despite the high variability, the model exhibited features similar to those observed consistently across macaques, including peaks at delta, theta/alpha, and beta frequencies. To quantify the variability and similarities and establish whether the LFP PSD generated by our model could be distinguished from that of macaques, we performed principal component analysis (PCA) (Figure 5B). PCA explained a large proportion of the variance (PC1 = 57%, PC2 = 14%). As can be observed, the cluster of model data points partly (11/25 data points) overlapped those of macaques 1 and 2, yielding them indistinguishable via PCA (circled green points in Figure 5B).

The mean PCA distance, calculated as the mean of the Euclidean distance between each pair of points between two clusters, provides a measure of the variability between the datasets. The mean PCA distance within each cluster for macaques was higher than that of the model (macaques mean ± SD = 1.1 ± 0.2, model = 0.6). This supports the observation that the 10-s LFP PSDs within each experimental session have similar or more variability than those generated by the model. The mean PCA distance between macaque 3 days 1 and 2 (1.3) was lower than between different macaques (1.6 ± 0.3). This supports the intuitive notion that variability was higher across different animals than within the same animal across days, which in turn was higher than the variability within each recording session. Interestingly, there were several examples of the mean PCA distance between the model and macaque sessions being lower than between macaque sessions (e.g., model vs. macaque 2 = 1.3; macaque 2 vs. macaque 3 [day 1] = 2.2), demonstrating the similarities between the model

and experimental spontaneous LFP PSDs. Further validation was provided by plotting a shuffled version of the model LFP PSDs, which appeared as a clearly separate cluster with no overlap with the macaque data (with the exception of one outlier). The correlation matrix (Figure 5C) across all LFP PSDs showed a very low correlation between the model and shuffled model data (−0.01 ± 0.12). Crucially, it also showed a much stronger mean correlation between the model and macaques than between the shuffled model and macaques (0.31 ± 0.28 vs. −0.04 ± 12; $p < 0.001$, rank-sum test).

Individual oscillation events were detected in CSD data from resting-state recordings gathered *in silico* from the A1 model and *in vivo* from macaques. The analysis was performed using the OEvent software, which has previously been used to detect and quantify features of oscillation events in human and macaque electrophysiology recordings.[61] Once identified, oscillation events were classified according to frequency band: delta (0.5–4 Hz), theta (4–9 Hz), alpha (9–15 Hz), beta (15–29 Hz), and gamma (30–80 Hz). Oscillation events were then sorted once more based on their laminar location, in either the supragranular, granular, or infragranular layers. We were thus able to compare model and experiment oscillation events that occurred in the same regions of the cortical column within the same frequency band. Examples of matching individual oscillation events from each frequency band are shown in Figure 6A.

Several features were used to compare oscillation events across model and experimental data from different frequency bands, including temporal duration, peak frequency, and number of cycles in the oscillation (Figure 6B). Overall, these three features showed similar average values and overlapping distributions when compared across the model and experiment and across cortical layers. Duration was the most consistent value, with close average values across model and experiment at all frequency bands ($p > 0.05$, t test). Average peak frequency did not show significant differences for most frequency bands ($p > 0.05$, t test), with the exception of (1) theta, which showed a slightly lower average frequency compared to the macaque experimental data ($p < 0.05$, t test), and (2) gamma, which showed a slightly higher average frequency compared to experiments ($p < 0.05$, t test). Similarly, the model average number of cycles per oscillation event was not significantly different to experimental values across frequency bands ($p > 0.05$, t test) with the exception of gamma, which showed a slightly higher average value ($p < 0.05$, t test). The minor discrepancies in average values may, however, represent an artifact due to the short overall duration of simulations (25 × 10 s) compared to the duration of macaque experimental recordings, which were on the order of minutes.

Unraveling the biophysical mechanisms underlying physiological oscillations at the cellular and circuit scales

After verifying that the oscillation events detected in the model data were comparable to the events observed in the macaque data, we harnessed the model to examine the cellular- and circuit-level activity underlying these oscillation events. This underscores one of the model's advantages: beyond generating comparable LFP and CSD data, its biological detail facilitates exploration of each population's contribution to shaping overall LFP and CSD signals. Furthermore, we were able to examine the spiking activity of each population during

each oscillation event, mirroring multiunit activity from neurophysiological recordings, but with enhanced cell-type specificity. As LFP/CSD signals predominantly originate from synaptic transmembrane currents, we adapted an existing method[62] to estimate the cell-type-specific synaptic inputs driving the different populations and the oscillatory patterns within these inputs. This facilitates predictions about the most likely biophysical sources of LFP/CSD oscillatory events in terms of the oscillatory synaptic inputs generating them.

We illustrate this approach using an LFP/CSD beta oscillation event detected in the macaque A1 infragranular layer data and a similar oscillation event detected in the A1 model infragranular layer (Figure 7A). To determine the biophysical circuit sources underlying this oscillation event, we calculated the contribution from each model population to the CSD signal, which was recorded from an electrode at depth 1,900 mm (Figure 7B). This revealed that the layer 6 corticothalamic population (CT6) was by far the primary contributor to the CSD event amplitude, followed by the layer 6 intratelencephalic population (IT6). Consistent with this observation, analysis of the CSD signals generated by the CT6 and IT6 populations during the overall beta oscillation event uncovered oscillation events with similar beta oscillation frequencies (~15–20 Hz range) and amplitude (~5–10 mV/mm^2) (Figure 7C). We then analyzed the CT6 and IT6 spiking activity during the oscillation event, which revealed a distinct CT6 oscillation in the same beta frequency range (Figure 7D). This evidenced spike-field coherence, with peak firing times of the CT6 neural population aligning with peaks in the CSD beta rhythm. No clear beta oscillation was observed in IT6 spiking activity.

Considering that synaptic currents primarily underlie LFP/CSD signals, we proceeded to analyze the synaptic inputs driving the CT6 and IT6 populations during the CSD beta oscillation event. This analysis leverages our ability to access the exact spiking activity and connectivity of all neurons to reveal the synaptic input patterns from different presynaptic populations. Our methodology for estimating synaptic drive is depicted in Figure 7E and described in STAR Methods, which also outlines its limitations.

Both CT6 and IT6 received strong synaptic inputs from the PV5A population, exhibiting a beta oscillatory pattern in the 15–20 Hz range. This suggests that the synaptic currents in CT6 and IT6 triggered by PV5A presynaptic inputs may underpin the CSD beta oscillation event (Figure 7F). The strong beta synaptic inputs to IT6 explain how this population could contribute significantly to the overall CSD beta oscillation (via their transmembrane synaptic currents) despite not displaying spiking activity in the beta range. While CT6 and IT6 also received strong oscillatory inputs from PV6, these were in the gamma frequency range, and thus appear unrelated to the beta oscillation. The presence of coincident beta and gamma demonstrates a cross-frequency interaction often observed in neural oscillations[63] and highlights how the model can be used to make predictions and disentangle the origins of the complex cortical dynamics observed *in vivo*.[64]

As a final step, we decided to explore the origins of the PV5A beta oscillatory activity employing the same synaptic input analysis approach. This unveiled a robust synaptic input beta oscillatory pattern in PV5A originating from the IT5B population (Figure 7F). In turn, analysis of IT5B synaptic inputs revealed a strong beta oscillatory input from PV5A and

PV5B. In summary, we traced back the source of the CSD beta oscillation event to the synaptic currents in CT6 and IT6 originating from PV5A inputs, which in turn appear to result from beta-band recurrent oscillatory interactions between PV5A and IT5B (see schematic, Figure 7G). This demonstrates the potential utility of the model in identifying the key biophysical circuit elements underlying electrophysiological activity patterns.

Figure S5 provides an additional example revealing further insights into how neural populations interact to generate spontaneous LFP/CSD oscillatory events. Here, we analyzed a CSD theta oscillation event detected in the A1 model supragranular layer (Figure S5A), similar to those detected in the macaque A1 data (Figure 6A). Analysis of the population CSD signals during the event demonstrated that the layer 4 stellate (ITS4), layer 4 pyramidal tract (ITP4), and layer 5A intratelencephalic (IT5A) neural populations made the strongest contributions to the amplitude of the theta CSD event (Figure S5B). Consistent with the model prediction, the dominant CSD peak frequencies of these three populations were very similar to that of the overall theta oscillation event: overall, 6.5 Hz (Figure S5A); ITS4, 6.75 Hz (Figure S5C); ITP4, 6.75 Hz (Figure S5D); IT5A, 7 Hz (Figure S5E). Interestingly, the individual population CSDs were not perfectly phase aligned; specifically, the IT5A signal (Figure S5E) appeared to be shifted by approximately 10–20 ms with respect to the layer 4 populations (Figure S5C,D). Although here we are only showing the top three contributing populations, other contributing populations also exhibited similar CSD signal phase shifts. We hypothesize that these phase shifts are responsible for the increased noise observed in the overall CSD signal compared to the individual population CSD signals that generated it. This increased noise may in turn explain the small differences in the CSD peak frequencies observed between the overall signal and the population signals that composed it. The contribution of IT5A to the overall CSD signal recorded at channel 8 is particularly interesting, given that the IT5A cell somas are located at a cortical depth of 1,250–1,350 μm whereas the channel 8 signals arise from electrodes at a depth of 700–900 μm. This suggests that IT5A apical dendrite currents generate a substantial component of the detected CSD theta oscillation.

DISCUSSION

Key findings and contributions

We have developed a detailed multiscale model of macaque auditory thalamocortical circuits, including MGB, TRN, and A1, and validated it against *in vivo* experimental data. The model integrated experimental data on the physiology, morphology, biophysics, density, laminar distribution, and proportion of different cell types, as well as their local and long-range synaptic connectivity (Figures 1 and 2). Realistic auditory inputs can be provided to the thalamus via a phenomenological model of the cochlear nucleus, auditory nerve, and IC. The model generated cell-type- and layer-specific firing rates in the ranges observed experimentally and simulated the corresponding measures at multiple scales: LFPs, laminar CSD analysis, and EEG (Figure 3). We identified multiple laminar CSD patterns during spontaneous activity and responses to BBN train stimuli similar to those recorded experimentally (Figure 4). Physiological oscillations emerged across frequency bands without external rhythmic inputs and were comparable to those recorded spontaneously *in*

vivo. Despite significant variability across animals and over time, the spectral power showed peaks at delta, theta/alpha, and beta frequencies in all animals and in the model (Figure 5). Additionally, individual CSD oscillation events closely matched physiological examples in all frequency bands (Figure 6A), and statistics on simulated CSD oscillation event duration, peak frequency, and number of cycles were consistent across layers and frequency bands with those reported *in vivo* (Figure 6B). We used the model to make predictions about the cellular and circuit biophysical mechanisms underlying specific oscillation events (Figure 7). Notably, the model disentangled the contribution of distinct neuronal population oscillatory activity and identified the synaptic transmembrane currents and key presynaptic populations involved. For example, the model predicted that the CSD beta oscillation event in Figure 7A was caused predominantly by synaptic input currents to CT6 and IT6 neurons, originating from the PV5A neurons through its recurrent interaction with IT5B neurons. Taken together, our findings underline the significant role played by modeling when interpreting the basic properties of *in vivo* electrophysiology data.

Although circuit models of similar size and complexity have been developed, these models have largely focused on rodent visual[40] and somatosensory[39] cortices. A highly detailed rat somatosensory cortex model was used to study stimulus-specific adaptation in the auditory cortex by modifying thalamic inputs,[65] but the overall model cortical architecture and connectivity was not adapted to replicate the particularities of auditory circuits or the macaque species. Compared to our model, previous models of auditory cortex lack significant detail in terms of neuron model complexity, range of cell types, neuronal density and distribution, and/or circuit connectivity.[66–70]

In short, the main contribution of this work is a model that: (1) incorporates available data specific to the macaque species and auditory cortex; (2) includes a wide range of excitatory and inhibitory cell types from both cortical and thalamic regions; (3) uses synaptic connectivity that is cell-type specific and layer specific, and includes bidirectional thalamic connections with distinct core and matrix projections; (4) simulates realistic auditory inputs through a cochlear and IC model; (5) generates realistic multiscale measures, including spiking activity, LFP, CSD, and EEG; (6) recapitulates a range of macaque A1 *in vivo* results; and (7) can be used to predict the biophysical mechanisms underlying observed neural responses, including oscillatory patterns.

Limitations of the study

Due to gaps in experimental data and in our theoretical understanding of biological principles, the model is necessarily incomplete and inaccurate and will need to be revised as more *in vivo* data become available. This is particularly true for the non-human primate auditory system, which has been less studied and is not as well characterized as, for example, the rodent visual system. Specifically, the availability of electrophysiological and connectivity data from the macaque auditory system for the different cortical and thalamic cell types was limited, so, when required, we used data from other macaque regions or from other mammalian auditory systems. Validating the layer- and cell-type-specific firing rates was also challenging, due to the lack of macaque A1 data; thus, many of the comparisons to experiments rely on the readily available laminar LFP and CSD measures. Despite these

limitations, we believe our model incorporates more properties specific to macaque A1 and has been validated against more macaque A1 data than any previous model. Furthermore, it can be iteratively improved and further validated as newer and more precise data become available.

Generating physiologically constrained firing rates in all model populations required parameter tuning (also referred to as parameter fitting or optimization) of the connection strengths within biologically realistic ranges. Compared to our previous motor cortex model,[62,71] this process was particularly challenging in the non-human primate auditory system model and required developing and iteratively improving our automated parameter optimization methods. We believe the reasons for this include the addition of two inhibitory cell types (VIP and NGF) and the incorporation of thalamic circuitry, which resulted in complex recurrent intracortical and thalamocortical interactions. The optimization methods resulted in a range of distinct model parameter combinations that produced valid network dynamics, a phenomenon known as parameter degeneracy. It is well known that biological neural circuits exhibit this same property: different combinations of neuron intrinsic and synaptic properties—each varying up to several orders of magnitude—can result in the circuit exhibiting the same physiological and functional outcome.[47]

In this initial iteration of the model, we did not include short-term facilitation and depression because of the increased complexity they would introduce to the parameter optimization process. We recognize this omission as a limitation, particularly when aiming to replicate *in vivo* circuit dynamics and functions, such as sensory input adaptation. For future model enhancements, the Neocortical Microcircuit Collaboration portal[72] offers a valuable resource to parameterize these short-term dynamics of neocortical synaptic connections.

The relatively narrow diameter (200 μm) of our simulated cortical column did not allow for a detailed implementation of the tonotopic organization of thalamic inputs. Nonetheless, the A1 column was tuned to a specific best frequency as determined by the filtering of inputs through the cochlear and IC model. The A1 column also received a realistic number of afferent core and matrix thalamic inputs, with layer specificity and cell-type specificity. Future model versions can be extended to have a larger-diameter column, or multiple columns, each receiving distinct thalamic projections, enabling the studying of circuit mechanisms that support frequency discrimination of auditory stimuli. Hence, in this study we did not attempt to reproduce BBN stimulus trains and speech responses in detail and instead focused on reproducing features of spontaneous activity, including the high variability observed experimentally.

We also simulated EEG signals based on the current dipoles of individual neurons in the macaque auditory cortical circuit model. Calculating the voltage at the different scalp electrodes requires a realistic head volume conduction model. Unfortunately, we did not find a macaque head model and resorted to using the standard human head model available within the LFPy tool.[54] This served as additional proof of concept of the ability of our model to simulate multiscale signals.

Outlook on research and clinical applications

Overall, the computational model provides a quantitative theoretical framework to integrate and interpret a wide range of experimental data, generate testable hypotheses, and make quantitative predictions. It constitutes a powerful tool to study the biophysical underpinnings of different experimental measurements, including LFP, EEG, and MEG.[73] This theoretical framework represents a baseline model that can be updated and extended as new data become available. Ongoing efforts by the BRAIN Initiative Cell Census Network and others may soon provide a cell census of the mammalian auditory cortex, similar to that recently made available for the motor cortex.[74] Our model is fully open source and implemented using the NetPyNE tool,[48] which was explicitly designed to facilitate integration of experimental data through an intuitive language focused on describing biological parameters. This will enable other researchers to readily adapt the model to reproduce experimental manipulations, e.g., chemogenetic or pharmacologic interventions, or dynamics associated with different brain diseases. Work is already ongoing to adapt the model to study the EEG correlates of schizophrenia in A1[75] and to evaluate a novel LFP recording device.[76] To facilitate interoperability with other tools, NetPyNE can also export the model to standard formats, such as NeuroML[77] and SONATA,[78] making it widely available to the community. Our detailed circuit model also incorporates naturalistic auditory inputs, allowing future research linking structure, dynamics, and function and providing insights into neural representations during naturalistic stimulus processing. Given the general similarities between non-human primate and human thalamocortical circuitry,[79,80] this data-driven model has high translational relevance and can start to bridge the gap across species and offer insights into healthy and pathological auditory system dynamics in humans.

STAR★METHODS

RESOURCE AVAILABILITY

Lead contact—Further information and requests for resources and reagents should be directed to and will be fulfilled by the lead contact, Salvador Dura-Bernal (salvador.dura-bernal@downstate.edu).

Materials availability—This study did not generate new materials. Links to the model source code, analysis code, experimental data and simulation data are available in the data and code availability subsection below.

Data and code availability—The model source code, analysis source code, experimental data to constrain and validate the model, and simulation output data used in this study are available via GitHub: https://github.com/NathanKlineInstitute/Macaque_auditory_thalamocortical_model_data and Zenodo: https://doi.org/10.5281/zenodo.10066993. The repository includes a detailed installation guide and system requirements, instructions for using the model and reproducing the figures, and a simplified demo of the model that can be simulated on desktop computers. The model source code is also available via ModelDB at https://modeldb.science/2014832. The model

is defined using the NetPyNE specifications, a JSON-based human-readable language, which can be exported to the SONATA and NeuroML standardized formats.

Any additional information required to simulate the model or analyze the data reported in this paper is available from the lead contact upon request.

METHOD DETAILS

We developed a model of the macaque auditory system consisting of a phenomenological model of cochlea and IC, and biophysically-detailed models of auditory thalamic and cortical circuits (Figure 1). We validated the model against macaque *in vivo* experimental data. This section details the modeling, experimental and analysis methods used.

Single neuron models

Morphology and physiology of neuron classes: The network includes conductance-based cell models with parameters optimized to reproduce physiological responses. We used simplified morphologies of 1–6 compartments for each cell type, and sized dendritic lengths to match macaque cortical dimensions (Figure 8.3/4.4 in Oliver et al.[81]). We fitted the electrophysiological properties of each cell type to extant electrophysiology data from macaque when available, or other animal models when it was not. Passive parameters, such as membrane capacitance, were tuned to fit resting membrane potential (RMP) and other features of subthreshold traces (e.g., sag from hyperpolarization). Active parameters included values such as the fast sodium channel density, and were tuned to reproduce characteristics like oscillatory bursting and firing rate vs. input current (f-I) curve (see Figure S1).

Within the A1 network, we modeled four classes of excitatory neurons: the intratelencephalic spiny stellate (ITS), intratelencephalic pyramidal (IT), pyramidal tract (PT) and corticothalamic (CT). These were distributed across the six cortical layers. The ITS model consisted of 3 compartments (a soma and 2 dendrites), and was adapted from a previously published layer 4 (L4) spiny stellate model.[82] There is evidence for the presence of stellate cells in A1 in mammals, including rodents, rabbits, bats, cats and humans,[45,81,83,84] although in some species these were relatively rare compared to visual and somatosensory cortices. Several macaque studies also mention the role of A1 L4 stellate cells in receiving input from thalamus.[85–87] The IT, PT, and CT cell models were each composed of 6 compartments: a soma, axon, basal dendrite, and 3 apical dendrites. These models were based on previous work,[88] in which simplified cell models were optimized to reproduce subthreshold and firing dynamics observed *in vivo*.[89–91] Apical dendrite lengths were modified to match macaque cortical dimensions and layer-specific connectivity requirements. The classification of cortical neurons into IT, PT and CT was based not only on their projection targets, but also on their local connectivity, laminar location, morphology, intrinsic physiology and genetics.[45,92] Although the PT terminology may be confusing for A1, this cell class refers to subcerebral projection neurons, including brainstem, and has been previously used for non-motor cortical regions (A1, V1, S1).[45,92,93] PT neurons have also been labeled as “extratelencephalic” (ET), but this does not distinguish them from the also extratelencephalic CT neurons. In A1, a category of neurons described as “large

pyramidal cells" overlap significantly with features of the PT cell class: mostly occupy L5B, have thick-tufted morphologies reaching up to L1, are intrinsically bursting and project to brainstem, including inferior colliculus (IC), superior olivary complex and the cochlear nuclear complex.[93–96]

Four classes of inhibitory neurons (NGF, SOM, PV, VIP) were also simulated in the A1 network model. The vasoactive intestinal peptide (VIP) cell model was based on a previously published 5-compartment model,[97] whereas the somatostatin (SOM) and parvalbumin (PV) interneurons were based on published 3-compartment models.[98] Parameters such as dendritic length were modified to better fit extant cortical data regarding rheobase and f-I curve.[99] The neurogliaform (NGF) cell model was adapted from an existing model in rodent,[100] with soma compartment size modified to more closely match the geometry of NGF cells in monkeys.[35] Channel mechanisms, including A-type potassium and Ih currents, were also added to the soma compartment to replicate the electrophysiological characteristics (e.g., sag, f-I curve) described for these cell types in the literature.[35]

In thalamus, the modeled MGB contained thalamocortical (TC) cells, high-threshold thalamocortical cells (HTC), and local thalamic interneurons (TI). The TC and HTC cells were both single-compartment models capable of tonic and burst firing,[101] with the HTC model having the addition of a high-threshold T-type channel mechanism.[102] The locally inhibitory TI cells had 2 compartments (a soma and a dendrite) and were fitted to *in vitro* electrophysiology data recorded from lateral geniculate nucleus.[103–105] These cells were optimized to reproduce the oscillatory bursting observed in this cell type.[105] The thalamic reticular nucleus (TRN) contained the single-compartment inhibitory reticular (IRE) cells, with parameters also optimized to display this cell type's characteristic intrinsic rhythmicity.[106,107]

Thalamocortical circuit model populations

Auditory thalamus: Our auditory thalamus model included the medial geniculate body (MGB) and the thalamic reticular nucleus (TRN). The MGB was composed of two types of thalamocortical neurons (TC, HTC) and thalamic interneurons (TI). TRN was composed of reticular nucleus cells (IRE). The overall proportion of excitatory to inhibitory neurons was 3:1. For TC, TI and IRE cell types, we included two separate populations in order to capture the distinct connectivity patterns of the core vs. matrix thalamic circuits. Matrix populations were labeled with an "M" at the end: TCM, IREM, TIM. The proportion of core to matrix neurons was 1:1.[108] The density and ratio of the different thalamic populations was based on experimental data.[37,46] The resulting ratio of thalamic to cortical neurons was 1:17, consistent with published data.[38]

Auditory cortex: We modeled a cylindrical volume of the macaque primary auditory cortex (A1) with a 200 μm diameter and 2000 μm height (cortical depth) including 12,187 neurons and over 25 million synapses (Figure 1B). The cylinder diameter was chosen to approximately match the horizontal dendritic span of a neuron located at the center, consistent with previous modeling approaches.[39,40] Macaque cortical depth and layer boundaries were based on macaque published data.[41,42] The model includes 36 neural

populations distributed across the 6 cortical layers and consisting of 4 excitatory (IT, ITS, PT, CT), and 4 inhibitory types (SOM, PV, VIP and NGF). Details of the biophysics and morphology of each cell type are provided in the section above ("single neuron models"). The laminar distribution, cell density and proportion of each cell type were based on experimental data.[41,43–45] Layer 1 included only NGF cells. Layers 2 to 6 included IT, SOM, PV, VIP and NGF cells. Additionally, ITS cells were added to layer 4, PT cells to layer 5B, and CT cells to layers 5A, 5B and 6. The resulting number of cells in each population depended on the modeled volume, layer boundaries and neuronal proportions and densities per layer.

Thalamocortical circuit model connectivity

Connectivity parameters: connection probability and weight: We characterized connectivity in the thalamocortical circuit using two parameters for each projection: probability of connection and unitary connection strength. The probability of connection was defined as the probability that each neuron in the postsynaptic population was connected to a neuron in the presynaptic population. For example, if both pre- and postsynaptic populations have 100 neurons, a probability of 10% will result in an average of 1,000 connections (10% of the total 10,000 possible connections). The set of presynaptic neurons to connect to was randomly selected and autapses and multapses were not allowed. Given the neuronal morphologies were simplified to 6 or fewer compartments, we used a single synaptic contact for each cell-to-cell connection.

Unitary connection strength was defined as the EPSP amplitude in response to a spike from a single presynaptic neuron. Given that synaptic weights in NEURON are typically defined as a change in conductance (in uS), we derived a scaling factor to map unitary EPSP amplitude (in mV) to synaptic weights. To do this, we simulated an excitatory synaptic input to generate a somatic EPSP of 0.5 mV at each neuron segment. We then calculated a scaling factor for each neuron segment that converted the EPSP amplitude (mV) values used to define connectivity in NetPyNE into the corresponding NEURON synaptic weights (in uS). This resulted in the somatic EPSP response to a unitary connection input being independent of synaptic location, also termed synaptic democracy.[109] Evidence from CA1 pyramidal neurons shows that synaptic conductances increased with distance from soma, to normalize somatic EPSP amplitude of inputs within 300 mm of soma.[110] However, this effect is not evident in L5 cortical pyramidal neurons.[111] Nonetheless, scaling of synaptic conductances can be further justified in terms of accounting for dendritic filtering due to space-clamp artifacts, which distort the measured synaptic conductance at the soma.[112] A similar correction factor has been previously implemented in the Blue Brain Project somatosensory cortex (S1) model's pyramidal neurons.[39,72] Scaling factors calculated for PT cell apical tufts were very high and resulted in overexcitability in network simulations, given that each cell can receive hundreds of inputs that interact supralinearly.[113,114] We, therefore, thresholded all dendritic scaling factors to a maximum of 5.0 with respect to the soma.

Types of synapses—Excitatory synapses consisted of colocalized AMPA (rise, decay τ: 0.05, 5.3 ms) and NMDA (rise, decay τ: 15, 150 ms) receptors, both with reversal potentials

of 0 mV. The ratio of NMDA to AMPA receptors was 1:1,[115] meaning their weights were each set to 50% of the connection weight. NMDA conductance was scaled by $1/(1 + 0.28\ Mg \cdot e^{(-0062\ V)})$ with Mg = 1mM.[116] Inhibitory synapses from SOM to excitatory neurons consisted of a slow $GABA_A$ receptor (rise, decay τ: 2, 100 ms) and $GABA_B$ receptor, with a 9:1 ratio. Synapses from SOM to inhibitory neurons only included the slow $GABA_A$ receptor. Synapses from PV consisted of a fast $GABA_A$ receptor (rise, decay τ: 0.07, 18.2). Synapses from VIP included a different fast $GABA_A$ receptor (rise, decay τ: 0.3, 6.4),[117] and synapses from NGF included the $GABA_A$ and $GABA_B$ receptors with a 1:1 ratio. The reversal potential was 0 mV from AMPA and NMDA, −80 mV for all $GABA_A$ and −93 mV for $GABA_B$. The $GABA_B$ synapse was modeled using second messenger connectivity to a G protein-coupled, inwardly-rectifying potassium channel (GIRK).[118] The remaining synapses were modeled with a double-exponential mechanism.

This initial version of the model does not include short-term facilitation and depression, given the added complexity it would add to the parameter optimization process. We acknowledge this as a limitation of the model, especially in the context of replicating *in vivo* circuit dynamics and function, such as adaptation to sensory inputs. The Neocortical Microcircuit Collaboration portal[72] provides a useful resource to parameterize the short-term dynamics of neocortical synaptic connections in future model versions.

Connection delays—Connection delays were estimated as 2 ms to account for presynaptic release and postsynaptic receptor delays, plus a variable propagation delay calculated as the 3D Euclidean distance between the pre- and postsynaptic cell bodies divided by a propagation speed of 0.5 m/s. Conduction velocities of unmyelinated axons range between 0.5 and 10 m/s,[119] but here we chose the lowest value given that our soma-to-soma distance underestimates the non-straight trajectory of axons and the distance to target dendritic synapses.

Intra-thalamic connectivity—Intrathalamic connectivity was derived from existing rodent, cat and primate experimental and computational studies[40,108,120–122] (see Figure 2). More specifically, connection probabilities and unitary strength for TC→RE, RE→TC and RE→RE (both core and matrix populations) were largely based on a previous primate thalamus study[108] and validated with data from mouse ventrobasal thalamus[120] and cat MGBv.[40,108,120–122] No evidence was found for TC recurrent connections. Thalamic interneuron connectivity was derived from the same cat MGBv study, which provided the number of synaptic contacts for TI→TI, TI→TC and TC→TI, from which we estimated the probability of connection from each projection. We also verified that our model intra-thalamic connectivity was generally consistent with that of the Allen Brain Institute visual thalamocortical model.[40,122] Given that thalamic neuron models were single-compartment, no specific dendritic synaptic location information was included.

Intra-cortical connectivity—Connectivity within the A1 local circuit populations was defined as a function of pre- and postsynaptic cell type and layer. Given the overall lack of detailed cell type-specific connectivity experimental data for macaque A1, we used as a starting point the connectivity from two experimentally grounded mammalian cortical microcircuit modeling studies: the Allen Brain Institute (ABI) V1[40] and the Blue Brain

Project (BBP) S1.[39] We then updated the model connectivity with experimental data specific to macaque A1, when available, or simply mammalian A1.

Both studies included the projection-specific probability of connection and unitary connection strength parameters that we required for our model. However, the ABI V1 model had fewer excitatory (1) and inhibitory (3) broad cell types than our A1 model (4 E and 4 I), whereas the BBP S1 model included significantly more (11 E and 15 I). Neither model included the distinction between L5A and L5B present in our A1 model. The ABI V1 did provide length constants to implement distance-dependent connectivity, which we wanted to include for some of the A1 projections. Therefore, as a first step, we mapped our cell types to the closest ones in the ABI V1 model and obtained the corresponding connectivity matrices for A1. We then updated the A1 connectivity of cell types that were missing from ABI V1 based on data from BBP S1, more specifically, the ITS, PT, CT and VIP cell types. To do this we mapped A1 cell types to those closest in BBP S1, and scaled the connectivity parameters of missing cell types proportionally, using shared cell types as reference (e.g., IT or PV). Through this systematic approach we were able to combine data from ABI V1 and BBP S1 in a consistent way, to determine the connectivity parameters of all the A1 populations.

Inhibitory connections were further refined using data from A1[94,117,123] or from studies with more detailed cell type-specific data.[42,124] We updated the L2/3 SOM connectivity so they projected strongly not only to superficial layer excitatory neurons, but also to deeper ones by targeting their apical dendrites; this was not the case for PV cells, which projected strongly mostly to intralaminar excitatory neurons.[123,124] More specifically, probabilities of connection from L2/3 SOM and PV to excitatory neurons were a function of the postsynaptic neuron layer (L1-L6) based on data from an A1 study.[123] The probability of connection from VIP to excitatory neurons was set to a very low value derived from mouse A1 data.[117] Following this same study, VIP→SOM connections were made strong, VIP→PV weak, and VIP→VIP very weak. Connection probabilities of all I → E/I projections decayed exponentially with distance using a projection-specific length constant obtained from the ABI V1 study.

Information on the dendritic location of synaptic inputs was also incorporated, when available, into the model. Cortical excitatory synapses targeted the soma and proximal dendrites of L2–4 excitatory neurons, distal dendrites of L5–6 excitatory neurons, and were uniformly distributed in cortical inhibitory neurons.[40,45,94] L1 NGF neurons targeted the apical tuft of excitatory neurons, L2–4 NGF targeted the apical trunk of L2–4 excitatory neurons and the upper trunk of L5–6 excitatory neurons, and L5–6 NGF targeted the lower trunk of L5–6 excitatory neurons.[42,94,124] Synapses from SOM interneurons were uniformly distributed along excitatory neurons, those from PV and VIP neurons targeted the soma and proximal dendrites of excitatory neurons.[42,123,124]

Thalamocortical and corticothalamic connectivity: Thalamocortical connections were layer- and cell type-specific and were derived from studies in mouse auditory cortex[125] and rodent somatosensory cortex.[120,126] Core MGB thalamocortical neurons projected to cortical excitatory neurons in cortical layers 3 to 6. The strongest projections were to layer

4 ITP, ITS and PV neurons. Weaker thalamocortical projections also targeted L3 IT and PV; L4 SOM and NGF; L5–6 IT, CT and PV; and L5B PT and SOM. Matrix thalamocortical neurons projected to excitatory neurons in all layers except 4, and to L1 NGF, L2/3 PV and SOM, and L5–6 PV. Core thalamic inputs targeted the soma and proximal dendrites of cortical excitatory cells, whereas matrix thalamic inputs targeted their distal dendrites.[108,122]

Corticothalamic projections originating from L5A, L5B and L6 CT neurons targeted all core thalamus populations (TC, HTC, TI and IRE); whereas projections from L5B IT and PT neurons targeted the matrix thalamus populations (TCM, TIM, IREM). Connectivity data was derived from primate and rodent studies on auditory cortex and other cortical regions.[45,94,108,122,127,128]

Background inputs—To model the influence of the other brain regions not explicitly modeled on auditory cortex and thalamus, we provided background inputs to all our model neurons. These inputs were modeled as independent Poisson spike generators for each cell, targeting apical excitatory and basal inhibitory synapses, with an average firing rate of 40 Hz. Connection weights were automatically adjusted for each cell type to ensure that, in the absence of local circuit connectivity, all neurons exhibited a low spontaneous firing rate of approximately 1 Hz.

Full model synaptic weight tuning

Overview of approach: Although we followed a systematic data-driven approach to build our model, the complete experimental dataset required to build a detailed model of the macaque auditory thalamocortical system is currently not available. Therefore, we had to combine experimental data from different species, different brain regions and obtained using different recording techniques. It is therefore not surprising that in order to obtain physiologically constrained firing rates across all populations, we needed to tune the connectivity parameters. Automated optimization methods have been previously used for simpler networks e.g., recurrent point-neuron spiking networks.[129–133] However, optimization of large-scale biophysically-detailed networks typically requires expert-guided parameter adjustments,[39,100] for example through parameter sweeps (grid search).[40] In order to find a more systematic approach to tune this type of model, here we explored automated optimization methods, and gradually refined them and combined them with heuristic approaches as needed. Here we describe the final approach employed to obtain the tuned network.

Automated optimization algorithm: Our starting point was the network with cell type-specific background inputs adjusted so that all cells fired at approximately 1 Hz in the absence of connectivity. We then added intracortical and thalamocortical connectivity with parameters taken from the literature and similar existing models. In the resulting network, before tuning the connectivity parameters, many of the populations were silent (0 Hz) or fired at very high rates (>100 Hz). We aimed to obtain a baseline network where all population average firing rates were in range with experimental recordings.

We initially attempted to tune the network using classic parameter grid search methods, but failed to obtain good solutions. After evaluating several automated optimization approaches,

we settled on the Optuna package (http://optuna.org),[134] a hyperparameter optimization framework designed for machine learning applications. This framework uses by default a tree-structured parzen estimator to dynamically search the parameter space. Compared to evolutionary algorithms, which we had used in the past, Optuna has the advantage of not requiring all candidates of a generation to be completed before moving to the next generation. Instead, it dynamically decides the next candidate to explore based on all the candidates evaluated up to that point, which makes it faster and less resource-consuming, while providing solutions with similar fitness values.

In order to automatically evaluate each candidate network we defined an objective function that quantified the fitness error based on the network population average firing rates. Specifically, by minimizing this objective function we aimed to obtain a network where all 43 cortical and thalamic neural populations produced physiological firing rates (Figure S2). We, therefore, defined an objective function that increased exponentially with the difference between each model population's measured and target firing rate. We multiplied this difference by a constant that dictated the rate of growth of the exponential function. We broadly defined the target physiological firing rates based on experimental[50–53] as 5 Hz for excitatory populations and 10 Hz for inhibitory populations, with exponential rate of growths of 1/20 Hz and 1/30 Hz, respectively. Given the large number of populations, we purposely kept the fitness function relatively relaxed to facilitate finding solutions. For example, excitatory populations firing at 5 Hz, 25 Hz and 100 Hz would generate a fitness error of 1 ($=e^{(5-5)/20}$), 2.7 ($=e^{(25-5)/20}$) and 116 ($=e^{(100-5)/20}$), respectively. We defined the overall fitness error as the mean fitness error across populations. To avoid extremely large values from individual populations dominating the overall error fitness, we set the maximum fitness error per population to 1000. To avoid silent populations we set a minimum required firing rate of 0.05 Hz, below which the fitness error was directly set to 1000. Finally, to ensure a relative homogeneity of the firing rates over the 1000 ms simulations, we evaluated this function separately over four consecutive 250 ms periods and averaged the result. This avoided solutions where, for example, a population exhibited the target firing rate, but fired strongly only during the first 100 ms and was silent for the remaining time. We therefore formally defined the objective function to be minimized as $\text{objective function} = 1/(N_p \cdot N_t) \cdot \sum_{p=1..Np} \sum_{i=1..Nt} \min\left(e^{|r(p,i) - t(p,i)|/s(p,i)}, fit_{max}\right)$ if $r(p,i) \geq m(p)$ else fit_{max}, where N_p is the number of neural populations, N_t is the number of time periods that are evaluated, p is the population index, i is the time period index, $r(p,i)$ is the average firing rate for population with index p during time period with index i, $t(p,i)$ and $s(p,i)$ are the target rate mean and exponential rate of growth for population p and time period with index i, and fit_{max} is the maximum (worst possible) fitness value.

We note that the objective function used to optimize the baseline model parameters did not include any features of oscillatory patterns or local field potential (LFPs). Hence, the vivo LFP oscillatory patterns reproduced by the model were not used in any way to train or optimize the model, only to validate the model predictions.

Layer-specific and cell-type specific parameters: To reduce the fitness errors, we gradually included more tuning parameters (see Figure S2). Our final approach included

4 projectionclass weight gains (E→E, E→I, I→E, I/I) for each of the 7 layers (1, 2, 3, 4, 5A, 5B, 6). The analysis also revealed the highly specific dynamics for each of the four inhibitory cell types, which prompted us to include inhibitory cell type-specific weight gains: E→ PV, E→ SOM, E→ VIP, E→ NGF and PV→ E, SOM→ E, VIP→ E, NGF→ E. Including both layer-specific and cell type-specific parameters resulted in overall better solutions with lower fitness errors.

Stepwise layer-by-layer tuning: Increasing the number of parameters (dimensions) increases the size of the parameter space to explore, which increases the number of optimization trials (simulations) required to obtain a good solution, and increases the risk of getting stuck in local minima. There are two main ways to reduce the parameter space: 1) reducing the number of parameters, e.g., including only parameters for a subset of layers, or of projection types; and 2) reducing the range of parameter values explored, e.g., constraining these based on previous optimization results. Both of these solutions are implemented in the stepwise layer-by-layer tuning approach, reducing the massive HPC resources required to explore the large model parameter spaces.

To implement the layer-by-layer tuning approach, we first optimized the parameters within L4 alone. Once this layer achieved valid firing rates in all cell populations we added L3, and tuned the L3 connectivity parameters, while we kept L2 parameters within a small range of the previously obtained solution. We repeated this for L2, L5A, L5B, L6 and finally L1. Due to a small bug when tuning L2 and L3, once the full model was tuned, we retuned to L2 and L3 while keeping the rest of parameters within a small range (Figure S2). A similar layer-by-layer approach was followed to tune the Allen Brain Institute V1 model,[40] although they used a heuristic unidimensional grid search approach, whereas we employed an automated multidimensional dynamic search using Optuna.

Projection-specific weight tuning: Once we had obtained a reasonable solution for most model populations using the layer-by-layer approach, additional fine-tuning was required to improve the rate of specific populations. In particular, the SOM2 and SOM3 were 0 Hz and PV2 and VIP2 were firing too high (>100 Hz). The parameters explored did not appear to provide enough specificity to improve the rate of these populations without worsening some of the others. Therefore, we had to tune the weight gains of specific population-to-population projections, e.g., from IT2 to SOM2. Using Optuna, we optimized the weights of all projections targeting the populations with inadequate rates: PV2, SOM2, VIP2 and SOM3. This resulted in improved rates for these populations.

Final model: Our final network included all 43 thalamic and cortical populations firing within 0.1 and 25 Hz, i.e., no epileptic or silent populations. Due to the unprecedented scale and level of detail in the model, e.g., complex interaction between 4 interneuron types, we had to employ an exploratory approach evaluating several methods to tune the weights. Overall, this required over 500,000 simulations and over 5 million core hours on HPCs. The lessons learned during this process should facilitate the automated tuning of similar detailed models in the future.

Phenomenological models of peripheral auditory structures: To simulate spontaneous activity in our baseline model we used background white noise as inputs to our thalamic and cortical populations. However, in order to accurately simulate auditory stimuli input we also connected a model of peripheral auditory structures such as the auditory nerve (AN) and inferior colliculus (IC). To simulate these structures, we used phenomenological models that captured the signal transformations occurring in these regions.[60] These models produced outputs to drive the thalamocortical cells in the downstream, more biologically detailed portion of the auditory pathway model. The AN responses modeled here included several characteristic nonlinearities such as rate saturation, adaptation, and phase locking.[60,135] Outputs from the AN model were convolved and modulated with synaptic information and used as inputs to a phenomenological model of inferior colliculus (IC). Model neurons of the IC utilized different types of modulation transfer functions to capture both the spectral and amplitude modulation tuning observed in this structure.[60,135–137] These phenomenological models mitigated common encoding issues encountered at high frequencies and high sound levels, providing us with IC outputs that were useful throughout a broad range of frequencies and noise.[135]

The AN and IC models were implemented in MATLAB and are available within the UR_EAR 2.0 tool (see Figure S3). We used .wav files as input to this tool and obtained time-resolved IC firing rates. The model allowed customization of several options, including the cochlear central frequency and bandwidth. We saved the firing rates for different input sounds and converted these to spike times using a Python-based inhomogeneous Poisson generator.[138] We then used NEURON spike generators (VecStims) defined in NetPyNE to provide the IC spike times as input to the model thalamic populations.

Model building, simulation and optimization: We developed the computational model using the NetPyNE tool,[48] and ran all parallel simulations using NEURON 8.0[49,139] with a fixed time step of 0.05 ms. NetPyNE is a python package that provides a high-level interface to NEURON, and allows for the definition of complicated multiscale models using an intuitive declarative language focused on the biological parameters. NetPyNE then translates these specifications into a NEURON model, facilitates running parallel simulations, and automates the optimization and exploration of parameters using supercomputers. We executed our simulations primarily on Google Cloud and EBRAINS ICEI Fenix Infrastructure supercomputers using a Slurm-based cluster with 80-core compute nodes.[71] Some simulations were also run on XSEDE supercomputers Comet and Stampede, either using our own allocations or through the Neuroscience Gateway (NSG).[140] We used the NetPyNE software tool to design, execute, organize, and analyze the simulations, as well as to export our model to the SONATA[78] and NeuroML[77] standards.

Simulated recordings, data analysis and visualization

Spiking raster plot, firing rate statistics and voltage traces: The NetPyNE package[48] was used to record and analyze simulation output data, and to visualize spiking raster plots, firing rate statistics, and neuronal membrane voltage traces.

Local field potential (LFP): The extracellular or local field potential (LFP) was calculated from the neuron transmembrane currents based on volume conduction theory. For this we assumed that the model neurons are immersed in a homogeneous and isotropic medium, that is, it is the same in all positions and has the same electrical conductivity in all directions, sigma = 0.3 mS/mm. The extracellular potential at each electrode can then be calculated as the sum of transmembrane currents generated at each segment of each cell, divided by the distance between the segment and the electrode. Since we assume a homogeneous distribution along each cylindrical compartment, we can extend this approach from a point current source to a line-source approximation by integrating along the center axis of each somatic and dendritic cylindrical compartment (see Equation 6 in[54]). This approach has been previously described in detail and has been widely adopted.[54,55,141]

Simulated LFP electrode contacts were spatially distributed at 100 μm intervals along a vertical axis of the 2000 μm A1 column. Model LFP recording, analysis and visualization was performed using the NetPyNE package, which implements the method described above.

Current source density (CSD): We compared the in silico current source density (CSD) signals with *in vivo* data recorded from the supragranular, granular, and infragranular layers of A1 while macaques were at rest. CSD was calculated as the second spatial derivative of the LFP. CSD analysis and visualization was performed using the NetPyNE package.[48]

Current dipoles and electroencephalogram (EEG): The biophysical neurons responsible for generating the electroencephalogram (EEG) signals are at enough distance from the EEG scalp contacts that only the current dipole moments contribute to the recorded signal.[54,55] Therefore, we first need to compute the current dipole moments from the single neuron models in our circuit. The current dipole moment of a neuron can be calculated by multiplying the transmembrane current at each segment by the 3D coordinates of each segment's midpoint, and summing across all segments (see Equation 11 in[54]).

EEG signals can then be computed through forward modeling by combining the current dipole moments with a volume-conductor model for the head.[142] Volume-conductor models vary in terms of the complexity of their electrical conductivity spatial distribution. These range from the very simplified homogeneous model to the more detailed four-sphere head model, to finite element models (FEM) with anatomically-detailed head models. Here, we employed the New York Head model, a precise standardized adult human FEM head model.[56,57]

We used the LFPykit[54] python package for the implementation of the current dipole moment calculation and EEG forward modeling. We interfaced the NetPyNE modeling tool with LFPykit such that the required calculations were performed at each time step and stored within the NetPyNE standardized data structures.

Oscillation event detection: Using the OEvent package,[61] we generated Morlet wavelet spectrograms and their corresponding CSD waveforms to identify individual oscillation events occurring in spontaneous data, and to compare these events across *in vivo* and in silico contexts. OEvent extracted moderate/high-power events using 7-cycle Morlet wavelets

on non-overlapping 10 s windows.[73,143] We used linearly spaced frequencies (0.25 Hz frequency increments) ranging from 0.25–125 Hz. Power time-series of each wavelet transform were normalized by median power from the recording/simulation. We applied a local maximum filter to detect peaks in the spectrogram. Local peaks were assessed to determine whether their power exceeded a 4x median threshold to detect moderate-to high-power events. Frequency and time bounds around the peak were determined by including time and frequency values before/after, above/below peak frequency until power fell below the smaller of 0.5× maximum event amplitude and 4× median threshold. As shown in Figure 6, this produced a bounding box around each oscillation event that was used to determine frequency spread (minF to maxF), duration, and peak frequency (frequency at which maximum power is detected). We merged events when their bounding box overlapping area in the spectrogram exceeded 50% of the minimum area of each individual event. This allowed for the continuity of events separated by minor fluctuations below threshold. We then calculated additional features from this set of events, including the number of cycles (event duration x peak frequency). We classified events into standard frequency bands on the following intervals: delta (0.5–4 Hz), theta (4–9 Hz), alpha (9–15 Hz), beta (15–29 Hz), gamma (30–80 Hz). Classification was based on the frequency at which maximum power occurred during each event. The number of oscillation events detected per frequency band was: delta: N_{model} = 12; N_{exp} = 55, theta N_{model} = 44; N_{exp} = 126, alpha: N_{model} = 59; N_{exp} = 138, beta: N_{model} = 192; N_{exp} = 318, and gamma: N_{model} = 2359; N_{exp} = 1625. Absolute oscillation event numbers often differed between model and experiment datasets due to differences in recording length. These oscillation event analysis techniques yielded morphologically similar events between the simulated and macaque data (Figure 6). Non-normalized CSD data were used to validate and analyze the contributions of individual cell populations to the detected oscillation events (Figure 7).

Broadband noise stimulus generation and analysis: The broadband noise (BBN) stimulus sound wave was originally generated in MATLAB using a duration of 100 ms, sampling frequency of 100,000 Hz, and maximum amplitude of $1/\pi$. The signal power spectra was evaluated to ensure an homogeneous power distribution across frequencies. The signal was saved as a .wav file and used as sound input in both the macaque experiments and the model (Figures 4B–4D). The MATLAB code is available online (see data and code availability section).

The BBN sound wave was processed in the model via the phenomenological model of auditory nerve (AN) and inferior colliculus (IC), which generated as output the instantaneous IC firing rates. The best frequency used for AN/IC model was 5656 Hz, consistent with the macaque A1 data used for comparison. The model IC firing rates were subsequently converted to spike times and assigned to the IC spike generator (Vecstim) population within the NetPyNE auditory thalamocortical model. The IC population serves as input to the thalamic populations.

The CSD event-related potentials (ERPs) in Figure 4D were calculated by averaging the 300 ms of CSD signal across the BBN stimuli train trigger times. The experimental recording consisted of 122 stimulus events with trigger times ranging from 13.6 s to 89.2 s at intervals (SOA) of 624.5 ms. The model recording consisted of 11 events with trigger times ranging

from 2.5 s to 11.0 s at intervals (SOA) of 850 ms. CSD signals were averaged across a specific channel corresponding to either supragranular, granular or infragranular layer (experiment: channels 4, 10, 13; model: channels 6, 11, 12). Prior to averaging, CSD signals were smoothed using a bandpass filter in the 1–30 Hz range.

Analysis of synaptic input drive: We analyzed the synaptic inputs driving different populations to better understand changes in the sources of observed CSD oscillatory patterns. To do this we estimated the input strength from each presynaptic population to the target postsynaptic population. Note that to estimate synaptic drive we took advantage of the fact that the synaptic strength between two neurons is defined in the model as the somatic unitary postsynaptic potential (uPSP), in mV. Our modeling tool internally estimates the required peak synaptic conductance in nS to approximate the somatic uPSP, making all synapses similarly efficient independent of dendritic location (synaptic democracy). Therefore, we can estimate the synaptic drive between two neurons by multiplying the synaptic strength (uPSPs in mV) by the firing rate of the presynaptic cell. To get the total synaptic drive to each postsynaptic cell within a given time window, we estimated the synaptic drive from each presynaptic cell and summed it across the presynaptic population. The last step was to average across all cells of the target postsynaptic population. The final equation for estimated synaptic drive between two populations is shown below:

$$s_t = \frac{1}{N_{post}} \sum_{i=0}^{N_{post}} \sum_{j=0}^{N_{i,pre}} r_{j,t} w_{i,j}$$

where, s is the average estimated synaptic drive between a presynaptic and a postsynaptic population within time window t, N_{post} is the number of cells in the postsynaptic population, $N_{i,pre}$ is the number of cells in the presynaptic population that project to postsynaptic cell i, r_j is the number of spikes fired by cell j within time period t, and $w_{i,j}$ is the synaptic strength between presynaptic cell j and postsynaptic cell i (in mV, as it represents somatic uPSP).

In the specific analysis in Figures 7E and 7F, we used the methods above to calculate the spike-triggered average time histogram of estimated synaptic drives to the CT6, IT6, PV5A and IT5B postsynaptic populations. We analyzed the inputs for a time window of 180 ms preceding the postsynaptic spike and using a histogram bin size of 5 ms. To quantify the oscillatory patterns present in the presynaptic input time histogram signals, we computed their power spectral density using the Morlet wavelet transform method.

Experimental dataset: We used a dataset which included local field potentials invasively recorded from the primary auditory cortex (A1) of 4 female non-human primates (NHPs) as they sat quietly in a dark room with their eyes mostly open (previously described in[61]). In a subset of recordings, short sentences in the English language were presented at 80dB SPL. In both conditions, there were no behavioral requirements of the NHPs and no rewards were offered. Outside of the recording sessions, NHPs had full access to fluids and food.

All procedures were approved in advance by the Animal Care and Use Committee of the Nathan Kline Institute. NHP data was recorded during acute penetrations of A1 in

rhesus macaques weighing 5–8 kg, who had been prepared surgically for chronic awake electrophysiological recordings. Prior to surgery, each animal was adapted to a custom fitted primate chair and to the sound proofed recording chamber. Surgical preparation was performed under general anesthesia using aseptic techniques (for details see[144,145]). Briefly, to provide access to the brain, either Cilux (Crist Instruments) or Polyetheretherketone (PEEK; Rogue Research Inc.) recording chambers were positioned normal to the cortical surface of the superior temporal plane for orthogonal penetration of A1. These recording chambers and a PEEK headpost (used to permit painless head restraint) were secured to the skull with ceramic screws and embedded in dental acrylic. Each NHP was given a minimum of 6 weeks for post-operative recovery before behavioral training and data collection began.

During recordings, NHPs were head-fixed and linear array multielectrodes (23 contacts with 100, 125 or 150μm intercontact spacing, Plexon Inc.) were acutely positioned to sample all cortical layers of A1. Neuroelectric signals were continuously recorded with a sampling rate of 44 kHz using the Alpha Omega SnR system.

For NHP data analyses using current-source density (CSD) signals, CSD was calculated as the second spatial derivative of laminar local field potential. This was done to reduce potential issues related to volume conducted activity. To examine patterns of LFP/CSD activity in NHP recordings, we first determined the supragranular, granular, and infragranular layer depths for each macaque subject, as done previously.[146] In macaques, the determination of the supragranular, granular, and infragranular layer depths relied on functional demarcation of these regions based on responses to preferred modality stimuli. For each NHP subject, we examined an averaged CSD profile resulting from the presentation of a stimulus which provoked an excitatory response in A1 (e.g., clicks, best frequency tones). An early sink in this CSD profile indicated the presence of the granular layer, while source/sink pairs above and below the granular layer designated the presence of the supragranular and infragranular layers, respectively.

The animal names and recording dates used in the LFP PSD analysis of Figure 5 are as follows: Macaque 1: bu031032, 6/19/2019; Macaque 2: ma031032, 9/22/2020; Macaque 3 (Day 1): rb031032, 3/27/2018; Macaque 3 (Day 2): rb045046, 5/24/2018.

All the experimental data used in this study and its associated description are available online (see data and code availability).

QUANTIFICATION AND STATISTICAL ANALYSIS

The statistical details of our study can be found in the results main text and figure captions. Specifically, we included the statistical test used in the main text, in brackets, next to the reported value. Similarly the value of N is indicated either in the main text or in the corresponding figure caption. Significance was generally defined as $p < 0.05$ and statistically high significance as $p < 0.001$. As measures of dispersion and precision, we used either mean ± SD (standard deviation) or median ± IQR (interquartile range), as indicated in the main text. For statistical analysis we used the Numpy, Scipy and Pandas Python packages.

Supplementary Material

Refer to Web version on PubMed Central for supplementary material.

ACKNOWLEDGMENTS

Research was supported by NIDCD R01DC012947, NIBIB U24EB028998, NIDCD 5R01DC019979, NIMH P50MH109429, NIBIB U01EB017695, NIMH R01MH134118–01, NINDS RF1NS133972, NYS DOH01-C32250GG-3450000, NSF 190444, Army Research Office W911NF-19–1-0402, Army Research Lab Cooperative Agreement W911NF-22–2-0139, and ARO URAP supplement. The views and conclusions contained in this document are those of the authors and should not be interpreted as representing the official policies, either expressed or implied, of the Army Research Office or the US Government. The US Government is authorized to reproduce and distribute reprints for Government purposes, notwithstanding any copyright notation herein. We acknowledge the use of Fenix Infrastructure resources, which are partially funded from the European Union's Horizon 2020 research and innovation programme through the ICEI project under grant agreement no. 800858.

Inclusion and diversity

We support inclusive, diverse, and equitable conduct of research.

REFERENCES

1. Hamilton LS, Oganian Y, Hall J, and Chang EF (2021). Parallel and distributed encoding of speech across human auditory cortex. Cell 184, 4626–4639.e13. [PubMed: 34411517]
2. Matsumoto R, Imamura H, Inouchi M, Nakagawa T, Yokoyama Y, Matsuhashi M, Mikuni N, Miyamoto S, Fukuyama H, Takahashi R, and Ikeda A (2011). Left anterior temporal cortex actively engages in speech perception: A direct cortical stimulation study. Neuropsychologia 49, 1350–1354. [PubMed: 21251921]
3. Fontolan L, Morillon B, Liegeois-Chauvel C, and Giraud A-L (2014). The contribution of frequency-specific activity to hierarchical information processing in the human auditory cortex. Nat. Commun. 5, 4694. [PubMed: 25178489]
4. Gourévitch B, Le Bouquin Jeannès R, Faucon G, and Liégeois-Chauvel C (2008). Temporal envelope processing in the human auditory cortex: response and interconnections of auditory cortical areas. Hear. Res. 237, 1–18. [PubMed: 18255243]
5. Andéol G, Guillaume A, Micheyl C, Savel S, Pellieux L, and Moulin A (2011). Auditory efferents facilitate sound localization in noise in humans. J. Neurosci. 31, 6759–6763. [PubMed: 21543605]
6. Carlile S, Martin R, and McAnally K (2005). Spectral Information in Sound Localization. International Review of Neurobiology, 70 (Academic Press), pp. 399–434. [PubMed: 16472641]
7. Ahveninen J, Kopčo N, and Jääskeläinen IP (2014). Psychophysics and neuronal bases of sound localization in humans. Hear. Res. 307, 86–97. [PubMed: 23886698]
8. Tramo MJ, Shah GD, and Braida LD (2002). Functional role of auditory cortex in frequency processing and pitch perception. J. Neurophysiol. 87, 122–139. [PubMed: 11784735]
9. Tramo MJ, Cariani PA, Koh CK, Makris N, and Braida LD (2005). Neurophysiology and neuroanatomy of pitch perception: auditory cortex. Ann. N. Y. Acad. Sci. 1060, 148–174. [PubMed: 16597761]
10. Dykstra AR, Koh CK, Braida LD, and Tramo MJ (2012). Dissociation of detection and discrimination of pure tones following bilateral lesions of auditory cortex. PLoS One 7, e44602. [PubMed: 22957087]
11. Hyde KL, Peretz I, and Zatorre RJ (2008). Evidence for the role of the right auditory cortex in fine pitch resolution. Neuropsychologia 46, 632–639. [PubMed: 17959204]
12. Latinus M, McAleer P, Bestelmeyer PEG, and Belin P (2013). Norm-based coding of voice identity in human auditory cortex. Curr. Biol. 23, 1075–1080. [PubMed: 23707425]
13. Holmes E, and Johnsrude IS (2021). Speech-evoked brain activity is more robust to competing speech when it is spoken by someone familiar. Neuroimage 237, 118107. [PubMed: 33933598]

14. Merchant SN, and Rosowski JJ (2008). Conductive hearing loss caused by third-window lesions of the inner ear. Otol. Neurotol. 29, 282–289. [PubMed: 18223508]
15. Raveh E, Hu W, Papsin BC, and Forte V (2002). Congenital conductive hearing loss. J. Laryngol. Otol. 116, 92–96. [PubMed: 11827579]
16. Taniwaki T, Tagawa K, Sato F, and Iino K (2000). Auditory agnosia restricted to environmental sounds following cortical deafness and generalized auditory agnosia. Clin. Neurol. Neurosurg. 102, 156–162. [PubMed: 10996714]
17. Brody RM, Nicholas BD, Wolf MJ, Marcinkevich PB, and Artz GJ (2013). Cortical deafness: a case report and review of the literature. Otol. Neurotol. 34, 1226–1229. [PubMed: 23921932]
18. Cavinato M, Rigon J, Volpato C, Semenza C, and Piccione F (2012). Preservation of auditory P300-like potentials in cortical deafness. PLoS One 7, e29909. [PubMed: 22272260]
19. Baguley DM (2003). Hyperacusis. J R Soc Med. 96, 582–585. [PubMed: 14645606]
20. Zendel BR, Lagrois MÉ, Robitaille N, and Peretz I (2015). Attending to pitch information inhibits processing of pitch information: the curious case of amusia. J. Neurosci. 35, 3815–3824. [PubMed: 25740512]
21. Albouy P, Mattout J, Bouet R, Maby E, Sanchez G, Aguera PE, Daligault S, Delpuech C, Bertrand O, Caclin A, and Tillmann B (2013). Impaired pitch perception and memory in congenital amusia: the deficit starts in the auditory cortex. Brain 136, 1639–1661. [PubMed: 23616587]
22. Dimitrijevic A, Smith ML, Kadis DS, and Moore DR (2017). Cortical Alpha Oscillations Predict Speech Intelligibility. Front. Hum. Neurosci. 11, 88. [PubMed: 28286478]
23. Schroeder CE, Lakatos P, Kajikawa Y, Partan S, and Puce A (2008). Neuronal oscillations and visual amplification of speech. Trends Cognit. Sci. 12, 106–113. [PubMed: 18280772]
24. Giraud A-L, and Poeppel D (2012). Cortical oscillations and speech processing: emerging computational principles and operations. Nat. Neurosci. 15, 511–517. [PubMed: 22426255]
25. Ghitza O (2011). Linking speech perception and neurophysiology: speech decoding guided by cascaded oscillators locked to the input rhythm. Front. Psychol. 2, 130. [PubMed: 21743809]
26. Hirano Y, Oribe N, Onitsuka T, Kanba S, Nestor PG, Hosokawa T, Levin M, Shenton ME, McCarley RW, and Spencer KM (2020). Auditory Cortex Volume and Gamma Oscillation Abnormalities in Schizophrenia. Clin. EEG Neurosci. 51, 244–251. [PubMed: 32204613]
27. Spencer KM, Niznikiewicz MA, Nestor PG, Shenton ME, and McCarley RW (2009). Left auditory cortex gamma synchronization and auditory hallucination symptoms in schizophrenia. BMC Neurosci. 10, 85. [PubMed: 19619324]
28. Hirano S, Nakhnikian A, Hirano Y, Oribe N, Kanba S, Onitsuka T, Levin M, and Spencer KM (2018). Phase-Amplitude Coupling of the Electroencephalogram in the Auditory Cortex in Schizophrenia. Biol. Psychiatry. Cogn. Neurosci. Neuroimaging 3, 69–76. [PubMed: 29397081]
29. Gandal MJ, Edgar JC, Ehrlichman RS, Mehta M, Roberts TPL, and Siegel SJ (2010). Validating g oscillations and delayed auditory responses as translational biomarkers of autism. Biol. Psychiatr. 68, 1100–1106.
30. De Stefano LA, Schmitt LM, White SP, Mosconi MW, Sweeney JA, and Ethridge LE (2019). Developmental Effects on Auditory Neural Oscillatory Synchronization Abnormalities in Autism Spectrum Disorder. Front. Integr. Neurosci. 13, 34. [PubMed: 31402856]
31. Jochaut D, Lehongre K, Saitovitch A, Devauchelle AD, Olasagasti I, Chabane N, Zilbovicius M, and Giraud AL (2015). Atypical coordination of cortical oscillations in response to speech in autism. Front. Hum. Neurosci. 9, 171. [PubMed: 25870556]
32. Paciello F, Rinaudo M, Longo V, Cocco S, Conforto G, Pisani A, Podda MV, Fetoni AR, Paludetti G, and Grassi C (2021). Auditory sensory deprivation induced by noise exposure exacerbates cognitive decline in a mouse model of Alzheimer's disease. Elife 10, e70908. [PubMed: 34699347]
33. Lakatos P, O'Connell MN, Barczak A, McGinnis T, Neymotin S, Schroeder CE, Smiley JF, and Javitt DC (2019). The thalamocortical circuit of auditory mismatch negativity. Biol. Psychiatr. 87, 770–780.
34. Edgar JC, Khan SY, Blaskey L, Chow VY, Rey M, Gaetz W, Cannon KM, Monroe JF, Cornew L, Qasmieh S, et al. (2015). Neuromagnetic oscillations predict evoked-response latency delays

and core language deficits in autism spectrum disorders. J. Autism Dev. Disord. 45, 395–405. [PubMed: 23963591]

35. Povysheva NV, Zaitsev AV, Krö ner S, Krimer OA, Rotaru DC, Gonzalez-Burgos G, Lewis DA, and Krimer LS. (2007). Electrophysiological differences between neurogliaform cells from monkey and rat prefrontal cortex. J. Neurophysiol. 97, 1030–1039. [PubMed: 17122314]
36. Markov NT, Misery P, Falchier A, Lamy C, Vezoli J, Quilodran R, Gariel MA, Giroud P, Ercsey-Ravasz M, Pilaz LJ, et al. (2011). Weight consistency specifies regularities of macaque cortical networks. Cerebr. Cortex 21, 1254–1272.
37. Winer JA, and Larue DT (1996). Evolution of GABAergic circuitry in the mammalian medial geniculate body. Proc. Natl. Acad. Sci. USA 93, 3083–3087. [PubMed: 8610172]
38. Coen-Cagli R, Kanitscheider I, and Pouget A (2017). A method to estimate the number of neurons supporting visual orientation discrimination in primates. F1000Res. 6, 1752. [PubMed: 29333238]
39. Markram H, Muller E, Ramaswamy S, Reimann MW, Abdellah M, Sanchez CA, Ailamaki A, Alonso-Nanclares L, Antille N, Arsever S, et al. (2015). Reconstruction and Simulation of Neocortical Microcircuitry. Cell 163, 456–492. [PubMed: 26451489]
40. Billeh YN, Cai B, Gratiy SL, Dai K, Iyer R, Gouwens NW, AbbasiAsl R, Jia X, Siegle JH, Olsen SR, et al. (2020). Systematic Integration of Structural and Functional Data into Multi-scale Models of Mouse Primary Visual Cortex. Neuron 106, 388–403.e18. [PubMed: 32142648]
41. Kelly JG, and Hawken MJ (2017). Quantification of neuronal density across cortical depth using automated 3D analysis of confocal image stacks. Brain Struct. Funct. 222, 3333–3353. [PubMed: 28243763]
42. Tremblay R, Lee S, and Rudy B (2016). GABAergic Interneurons in the Neocortex: From Cellular Properties to Circuits. Neuron 91, 260–292. [PubMed: 27477017]
43. Lefort S, Tomm C, Floyd Sarria J-C, and Petersen CCH (2009). The Excitatory Neuronal Network of the C2 Barrel Column in Mouse Primary Somatosensory Cortex. Neuron 61, 301–316. [PubMed: 19186171]
44. Schuman B, Machold RP, Hashikawa Y, Fuzik J, Fishell GJ, and Rudy B (2019). Four Unique Interneuron Populations Reside in Neocortical Layer 1. J. Neurosci. 39, 125–139. [PubMed: 30413647]
45. Harris KD, and Shepherd GMG (2015). The neocortical circuit: themes and variations. Nat. Neurosci. 18, 170–181. [PubMed: 25622573]
46. Huang CL, Larue DT, and Winer JA (1999). GABAergic organization of the cat medial geniculate body. J. Comp. Neurol. 415, 368–392. [PubMed: 10553120]
47. Prinz AA, Bucher D, and Marder E (2004). Similar network activity from disparate circuit parameters. Nat. Neurosci. 7, 1345–1352. [PubMed: 15558066]
48. Dura-Bernal S, Suter BA, Gleeson P, Cantarelli M, Quintana A, Rodriguez F, Kedziora DJ, Chadderdon GL, Kerr CC, Neymotin SA, et al. (2019). NetPyNE, a tool for data-driven multiscale modeling of brain circuits. Elife 8, e44494. [PubMed: 31025934]
49. Lytton WW, Seidenstein AH, Dura-Bernal S, McDougal RA, Schürmann F, and Hines ML (2016). Simulation neurotechnologies for advancing brain research: parallelizing large networks in NEURON. Neural Comput. 28, 2063–2090. [PubMed: 27557104]
50. Wang X, Lu T, Snider RK, and Liang L (2005). Sustained firing in auditory cortex evoked by preferred stimuli. Nature 435, 341–346. [PubMed: 15902257]
51. Sakata S, and Harris KD (2009). Laminar structure of spontaneous and sensory-evoked population activity in auditory cortex. Neuron 64, 404–418. [PubMed: 19914188]
52. Eggermont JJ (1992). Stimulus induced and spontaneous rhythmic firing of single units in cat primary auditory cortex. Hear. Res. 61, 1–11. [PubMed: 1526882]
53. Hromádka T, Deweese MR, and Zador AM (2008). Sparse representation of sounds in the unanesthetized auditory cortex. PLoS Biol. 6, e16. [PubMed: 18232737]
54. Hagen E, Næss S, Ness TV, and Einevoll GT (2018). Multimodal Modeling of Neural Network Activity: Computing LFP, ECoG, EEG, and MEG Signals With LFPy 2.0. Front. Neuroinf. 12, 92.
55. Lindén H, Hagen E, Lę ski S, Norheim ES, Pettersen KH, and Einevoll GT. (2014). LFPy: A tool for biophysical simulation of extracellular potentials generated by detailed model neurons. Front. Neuroinf. 7, 41.

56. Huang Y, Parra LC, and Haufe S (2016). The New York Head-A precise standardized volume conductor model for EEG source localization and tES targeting. Neuroimage 140, 150–162. [PubMed: 26706450]
57. De Munck JC, Wolters CH, and Clerc M (2012). EEG and MEG: forward modeling. Handbook of neural activity measurement 19, 192–248.
58. Buzsáki G, Anastassiou CA, and Koch C (2012). The origin of extracellular fields and currents–EEG, ECoG, LFP and spikes. Nat. Rev. Neurosci. 13, 407–420. [PubMed: 22595786]
59. Rimehaug AE, Stasik AJ, Hagen E, Billeh YN, Siegle JH, Dai K, Olsen SR, Koch C, Einevoll GT, and Arkhipov A (2023). Uncovering circuit mechanisms of current sinks and sources with biophysical simulations of primary visual cortex. Elife 12, e87169. [PubMed: 37486105]
60. Krishna BS, and Semple MN (2000). Auditory temporal processing: responses to sinusoidally amplitude-modulated tones in the inferior colliculus. J. Neurophysiol. 84, 255–273. [PubMed: 10899201]
61. Neymotin SA, Tal I, Barczak A, O'Connell MN, McGinnis T, Markowitz N, Espinal E, Griffith E, Anwar H, Dura-Bernal S, et al. (2022). Detecting Spontaneous Neural Oscillation Events in Primate Auditory Cortex. eNeuro 9. ENEURO.0281, 21.2022.
62. Dura-Bernal S, Neymotin SA, Suter BA, Dacre J, Moreira JVS, Urdapilleta E, Schiemann J, Duguid I, Shepherd GMG, and Lytton WW (2023). Multiscale model of primary motor cortex circuits predicts in vivo cell-type-specific, behavioral state-dependent dynamics. Cell Rep. 42, 112574. [PubMed: 37300831]
63. Jensen O, and Colgin LL (2007). Cross-frequency coupling between neuronal oscillations. Trends Cognit. Sci. 11, 267–269. [PubMed: 17548233]
64. O'Connell MN, Barczak A, Ross D, McGinnis T, Schroeder CE, and Lakatos P (2015). Multi-Scale Entrainment of Coupled Neuronal Oscillations in Primary Auditory Cortex. Front. Hum. Neurosci. 9, 655. [PubMed: 26696866]
65. Amsalem O, King J, Reimann M, Ramaswamy S, Muller E, Markram H, Nelken I, and Segev I (2020). Dense Computer Replica of Cortical Microcircuits Unravels Cellular Underpinnings of Auditory Surprise Response. Preprint at bioRxiv. 10.1101/2020.05.31.126466.
66. Park Y, and Geffen MN (2020). A circuit model of auditory cortex. PLoS Comput. Biol. 16, e1008016. [PubMed: 32716912]
67. Stanley DA, Falchier AY, Pittman-Polletta BR, Lakatos P, Whittington MA, Schroeder CE, and Kopell NJ (2019). Flexible reset and entrainment of delta oscillations in primate primary auditory cortex: modeling and experiment. Preprint at bioRxiv. 10.1101/812024.
68. Loebel A, Nelken I, and Tsodyks M (2007). Processing of sounds by population spikes in a model of primary auditory cortex. Front. Neurosci. 1, 197–209. [PubMed: 18982129]
69. Zulfiqar I, Moerel M, and Formisano E (2019). Spectro-Temporal Processing in a Two-Stream Computational Model of Auditory Cortex. Front. Comput. Neurosci. 13, 95. [PubMed: 32038212]
70. Kudela P, Boatman-Reich D, Beeman D, and Anderson WS (2018). Modeling Neural Adaptation in Auditory Cortex. Front. Neural Circ. 12, 72.
71. Sivagnanam S, Gorman W, Doherty D, Neymotin SA, Fang S, Hovhannisyan H, Lytton WW, and Dura-Bernal S (2020). Simulating Large-scale Models of Brain Neuronal Circuits using Google Cloud Platform. In Practice and Experience in Advanced Research Computing (Association for Computing Machinery), pp. 505–509.
72. Ramaswamy S, Courcol JD, Abdellah M, Adaszewski SR, Antille N, Arsever S, Atenekeng G, Bilgili A, Brukau Y, Chalimourda A, et al. (2015). The Neocortical Microcircuit Collaboration Portal: A Resource for Rat Somatosensory Cortex. Front. Neural Circ. 9, 44.
73. Neymotin SA, Daniels DS, Caldwell B, McDougal RA, Carnevale NT, Jas M, Moore CI, Hines ML, Hä mä lä inen M, and Jones SR. (2020). Human Neocortical Neurosolver (HNN), a new software tool for interpreting the cellular and network origin of human MEG/EEG data. Elife 9, e51214. [PubMed: 31967544]
74. BRAIN Initiative Cell Census Network BICCN (2021). A multimodal cell census and atlas of the mammalian primary motor cortex. Nature 598, 86–102. [PubMed: 34616075]
75. Metzner C, and Steuber V (2021). The beta component of gamma-band auditory steady-state responses in patients with schizophrenia. Sci. Rep. 11, 20387. [PubMed: 34650135]

76. Abrego AM, Khan W, Wright CE, Rabiul Islam M, Ghajar MH, Bai X, Tandon N, and Seymour JP (2021). Sensing Local Field Potentials with a Directional and Scalable Depth Array: the DISC electrode array. Preprint at bioRxiv. 10.1101/2021.09.20.460996.
77. Gleeson P, Cantarelli M, Marin B, Quintana A, Earnshaw M, Sadeh S, Piasini E, Birgiolas J, Cannon RC, Cayco-Gajic NA, et al. (2019). Open Source Brain: A Collaborative Resource for Visualizing, Analyzing, Simulating, and Developing Standardized Models of Neurons and Circuits. Neuron 103, 395–411.e5. 10.1016/j.neuron.2019.05.019. [PubMed: 31201122]
78. Dai K, Hernando J, Billeh YN, Gratiy SL, Planas J, Davison AP, Dura-Bernal S, Gleeson P, Devresse A, Dichter BK, et al. (2020). The SONATA data format for efficient description of large-scale network models. PLoS Comput. Biol. 16, e1007696. [PubMed: 32092054]
79. Herculano-Houzel S (2009). The human brain in numbers: a linearly scaled-up primate brain. Front. Hum. Neurosci. 3, 31. [PubMed: 19915731]
80. Passingham RE (1973). Anatomical differences between the neocortex of man and other primates. Brain Behav. Evol. 7, 337–359. [PubMed: 4198522]
81. Oliver DL, Cant NB, Fay RR, and Popper AN (2018). The Mammalian Auditory Pathways: Synaptic Organization and Microcircuits (Springer).
82. Mainen ZF, and Sejnowski TJ (1996). Influence of dendritic structure on firing pattern in model neocortical neurons. Nature 382, 363–366. [PubMed: 8684467]
83. Meyer G, Gonzá lez-Herná ndez TH, and Ferres-Torres R. (1989). The spiny stellate neurons in layer IV of the human auditory cortex. A Golgi study. Neuroscience 33, 489–498. [PubMed: 2484005]
84. Wang Y, Brzozowska-Prechtl A, and Karten HJ (2010). Laminar and columnar auditory cortex in avian brain. Proc. Natl. Acad. Sci. USA 107, 12676–12681. [PubMed: 20616034]
85. Steinschneider M, Reser DH, Fishman YI, Schroeder CE, and Arezzo JC (1998). Click train encoding in primary auditory cortex of the awake monkey: evidence for two mechanisms subserving pitch perception. J. Acoust. Soc. Am. 104, 2935–2955. [PubMed: 9821339]
86. Steinschneider M, Tenke CE, Schroeder CE, Javitt DC, Simpson GV, Arezzo JC, and Vaughan HG Jr. (1992). Cellular generators of the cortical auditory evoked potential initial component. Electroencephalogr. Clin. Neurophysiol. 84, 196–200. [PubMed: 1372236]
87. Fishman YI, Reser DH, Arezzo JC, and Steinschneider M (2000). Complex tone processing in primary auditory cortex of the awake monkey. I. Neural ensemble correlates of roughness. J. Acoust. Soc. Am. 108, 235–246. [PubMed: 10923888]
88. Neymotin SA, Suter BA, Dura-Bernal S, Shepherd GMG, Migliore M, and Lytton WW (2017). Optimizing computer models of corticospinal neurons to replicate in vitro dynamics. J. Neurophysiol. 117, 148–162. [PubMed: 27760819]
89. Suter BA, Migliore M, and Shepherd GMG (2013). Intrinsic electrophysiology of mouse corticospinal neurons: a class-specific triad of spike-related properties. Cerebr. Cortex 23, 1965–1977.
90. Yamawaki N, Borges K, Suter BA, Harris KD, and Shepherd GMG (2014). A genuine layer 4 in motor cortex with prototypical synaptic circuit connectivity. Elife 3, e05422. [PubMed: 25525751]
91. Oswald MJ, Tantirigama MLS, Sonntag I, Hughes SM, and Empson RM (2013). Diversity of layer 5 projection neurons in the mouse motor cortex. Front. Cell. Neurosci. 7, 174. [PubMed: 24137110]
92. Shepherd GMG, and Yamawaki N (2021). Untangling the cortico-thalamo-cortical loop: cellular pieces of a knotty circuit puzzle. Nat. Rev. Neurosci. 22, 389–406. [PubMed: 33958775]
93. Baker A, Kalmbach B, Morishima M, Kim J, Juavinett A, Li N, and Dembrow N (2018). Specialized Subpopulations of Deep-Layer Pyramidal Neurons in the Neocortex: Bridging Cellular Properties to Functional Consequences. J. Neurosci. 38, 5441–5455. [PubMed: 29798890]
94. Budinger E, and Kanold PO (2018). Auditory Cortex Circuits. In The Mammalian Auditory Pathways: Synaptic Organization and Microcircuits, Oliver DL, Cant NB, Fay RR, and Popper AN, eds. (Springer International Publishing), pp. 199–233.
95. Winer JA, Chernock ML, Larue DT, and Cheung SW (2002). Descending projections to the inferior colliculus from the posterior thalamus and the auditory cortex in rat, cat, and monkey. Hear. Res. 168, 181–195. [PubMed: 12117520]

96. Winer JA, and Schreiner CE (2010). The Auditory Cortex (Springer Science & Business Media).

97. Turi GF, Li WK, Chavlis S, Pandi I, O'Hare J, Priestley JB, Grosmark AD, Liao Z, Ladow M, Zhang JF, et al. (2019). Vasoactive Intestinal Polypeptide-Expressing Interneurons in the Hippocampus Support Goal-Oriented Spatial Learning. Neuron 101, 1150–1165.e8. [PubMed: 30713030]

98. Konstantoudaki X, Papoutsi A, Chalkiadaki K, Poirazi P, and Sidiropoulou K (2014). Modulatory effects of inhibition on persistent activity in a cortical microcircuit model. Front. Neural Circ. 8, 7.

99. Tripathy SJ, Burton SD, Geramita M, Gerkin RC, and Urban NN (2015). Brain-wide analysis of electrophysiological diversity yields novel categorization of mammalian neuron types. J. Neurophysiol. 113, 3474–3489. [PubMed: 25810482]

100. Bezaire MJ, Raikov I, Burk K, Vyas D, and Soltesz I (2016). Inter-neuronal mechanisms of hippocampal theta oscillation in a full-scale model of the rodent CA1 circuit. Elife 5, e18566. [PubMed: 28009257]

101. Iavarone E, Yi J, Shi Y, Zandt BJ, O'Reilly C, Van Geit W, Rössert C, Markram H, and Hill SL (2019). Experimentally-constrained biophysical models of tonic and burst firing modes in thalamocortical neurons. PLoS Comput. Biol. 15, e1006753. [PubMed: 31095552]

102. Vijayan S, and Kopell NJ (2012). Thalamic model of awake alpha oscillations and implications for stimulus processing. Proc. Natl. Acad. Sci. USA 109, 18553–18558. [PubMed: 23054840]

103. Zhu JJ, Uhlrich DJ, and Lytton WW (1999). Burst firing in identified rat geniculate interneurons. Neuroscience 91, 1445–1460. [PubMed: 10391450]

104. Zhu JJ, Uhlrich DJ, and Lytton WW (1999). Properties of a hyperpolarization-activated cation current in interneurons in the rat lateral geniculate nucleus. Neuroscience 92, 445–457. [PubMed: 10408596]

105. Zhu JJ, Lytton WW, Xue JT, and Uhlrich DJ (1999). An intrinsic oscillation in interneurons of the rat lateral geniculate nucleus. J. Health.com 81, 702–711.

106. Destexhe A, Contreras D, Sejnowski TJ, and Steriade M (1994). A model of spindle rhythmicity in the isolated thalamic reticular nucleus. J. Neurophysiol. 72, 803–818. [PubMed: 7527077]

107. Destexhe A, Bal T, McCormick DA, and Sejnowski TJ (1996). Ionic mechanisms underlying synchronized oscillations and propagating waves in a model of ferret thalamic slices. J. Neurophysiol. 76, 2049–2070. [PubMed: 8890314]

108. Bonjean M, Baker T, Bazhenov M, Cash S, Halgren E, and Sejnowski T (2012). Interactions between core and matrix thalamocortical projections in human sleep spindle synchronization. J. Neurosci. 32, 5250–5263. [PubMed: 22496571]

109. Rumsey CC, and Abbott LF (2006). Synaptic democracy in active dendrites. J. Neurophysiol. 96, 2307–2318. [PubMed: 16837665]

110. Magee JC, and Cook EP (2000). Somatic EPSP amplitude is independent of synapse location in hippocampal pyramidal neurons. Nat. Neurosci. 3, 895–903. [PubMed: 10966620]

111. Williams SR, and Stuart GJ (2002). Dependence of EPSP efficacy on synapse location in neocortical pyramidal neurons. Science 295, 1907–1910. [PubMed: 11884759]

112. Spruston N, Jaffe DB, Williams SH, and Johnston D (1993). Voltage- and space-clamp errors associated with the measurement of electrotonically remote synaptic events. J. Neurophysiol. 70, 781–802. [PubMed: 8410172]

113. Spruston N (2008). Pyramidal neurons: dendritic structure and synaptic integration. Nat. Rev. Neurosci. 9, 206–221. [PubMed: 18270515]

114. Behabadi BF, Polsky A, Jadi M, Schiller J, and Mel BW (2012). Location-dependent excitatory synaptic interactions in pyramidal neuron dendrites. PLoS Comput. Biol. 8, e1002599. [PubMed: 22829759]

115. Myme CIO, Sugino K, Turrigiano GG, and Nelson SB (2003). The NMDA-to-AMPA Ratio at Synapses Onto Layer 2/3 Pyramidal Neurons Is Conserved Across Prefrontal and Visual Cortices. J. Neurophysiol. 90, 771–779. [PubMed: 12672778]

116. Jahr CE, and Stevens CF (1990). Voltage dependence of NMDA-activated macroscopic conductances predicted by single-channel kinetics. J. N. Sci. 10, 3178–3182.

117. Pi H-J, Hangya B, Kvitsiani D, Sanders JI, Huang ZJ, and Kepecs A (2013). Cortical interneurons that specialize in disinhibitory control. Nature 503, 521–524. [PubMed: 24097352]

118. Destexhe A, Babloyantz A, and Sejnowski TJ (1993). Ionic mechanisms for intrinsic slow oscillations in thalamic relay neurons. Biophys. J. 65, 1538–1552. [PubMed: 8274647]
119. Purves D, Augustine GJ, Fitzpatrick D, Hall WC, LaMantia AS, Mooney RD, Platt ML, and White LE (2018). Neuroscience, (Sixth Edition).
120. Cruikshank SJ, Urabe H, Nurmikko AV, and Connors BW (2010). Pathway-specific feedforward circuits between thalamus and neocortex revealed by selective optical stimulation of axons. Neuron 65, 230–245. [PubMed: 20152129]
121. Serkov FN, and Gonchar YA (1996). Morphometric characteristics of synaptic apparatus in the dorsal nucleus of the medial geniculate body of the cat. Neurophysiology 28, 155–163.
122. Jones EG (2002). Thalamic circuitry and thalamocortical synchrony. Philos. Trans. R. Soc. Lond. B Biol. Sci. 357, 1659–1673. [PubMed: 12626002]
123. Kato HK, Asinof SK, and Isaacson JS (2017). Network-Level Control of Frequency Tuning in Auditory Cortex. Neuron 95, 412–423.e4. [PubMed: 28689982]
124. Naka A, and Adesnik H (2016). Inhibitory circuits in cortical layer 5. Front. Neural Circ. 10, 35.
125. Ji X-Y, Zingg B, Mesik L, Xiao Z, Zhang LI, and Tao HW (2016). Thalamocortical Innervation Pattern in Mouse Auditory and Visual Cortex: Laminar and Cell-Type Specificity. Cerebr. Cortex 26, 2612–2625.
126. Constantinople CM, and Bruno RM (2013). Deep cortical layers are activated directly by thalamus. Science 340, 1591–1594. [PubMed: 23812718]
127. Yamawaki N, and Shepherd GMG (2015). Synaptic circuit organization of motor corticothalamic neurons. J. Neurosci. 35, 2293–2307. [PubMed: 25653383]
128. Crandall SR, Cruikshank SJ, and Connors BW (2015). A corticothalamic switch: controlling the thalamus with dynamic synapses. Neuron 86, 768–782. [PubMed: 25913856]
129. Nicola W, and Clopath C (2017). Supervised learning in spiking neural networks with FORCE training. Nat. Commun. 8, 2208. [PubMed: 29263361]
130. Sussillo D, and Abbott LF (2009). Generating coherent patterns of activity from chaotic neural networks. Neuron 63, 544–557. [PubMed: 19709635]
131. Dura-Bernal S, Neymotin SA, Kerr CC, Sivagnanam S, Majumdar A, Francis JT, and Lytton WW (2017). Evolutionary algorithm optimization of biological learning parameters in a biomimetic neuroprosthesis. IBM J. Res. Dev. 61, 6:1–6:14.
132. Carlson KD, Nageswaran JM, Dutt N, and Krichmar JL (2014). An efficient automated parameter tuning framework for spiking neural networks. Front. Neurosci. 8, 10. [PubMed: 24550771]
133. Hasxegan D, Deible M, Earl C, D'Onofrio D, Hazan H, Anwar H, and Neymotin SA (2022). Training spiking neuronal networks to perform motor control using reinforcement and evolutionary learning. Front. Comput. Neurosci. 16, 1017284. [PubMed: 36249482]
134. Akiba T, Sano S, Yanase T, Ohta T, and Koyama MO (2019). A Next-generation Hyperparameter Optimization Framework. In Proceedings of the 25th ACM SIGKDD International Conference on Knowledge Discovery & Data Mining 2623–2631 (Association for Computing Machinery).
135. Carney LH, Li T, and McDonough JM (2015). Speech Coding in the Brain: Representation of Vowel Formants by Midbrain Neurons Tuned to Sound Fluctuations. eNeuro 2. ENEURO.0004, 15.2015.
136. Nelson PC, and Carney LH (2004). A phenomenological model of peripheral and central neural responses to amplitude-modulated tones. J. Acoust. Soc. Am. 116, 2173–2186. [PubMed: 15532650]
137. Joris PX, Schreiner CE, and Rees A (2004). Neural processing of amplitude-modulated sounds. Physiol. Rev. 84, 541–577. [PubMed: 15044682]
138. Muller E, Buesing L, Schemmel J, and Meier K (2007). Spike-frequency adapting neural ensembles: beyond mean adaptation and renewal theories. Neural Comput. 19, 2958–3010. [PubMed: 17883347]
139. Carnevale NT, and Hines ML (2006). The NEURON Book (Cambridge University Press).
140. Sivagnanam S, Majumdar A, Yoshimoto K, Astakhov V, Bandrowski A, Martone M, and Carnevale N (2013). Introducing the Neuroscience Gateway. In s.

141. Gratiy SL, Billeh YN, Dai K, Mitelut C, Feng D, Gouwens NW, Cain N, Koch C, Anastassiou CA, and Arkhipov A (2018). BioNet: a Python interface to NEURON for modeling large-scale networks. PLoS One 13, e0201630. [PubMed: 30071069]

142. Næss S, Halnes G, Hagen E, Hagler DJ Jr., Dale AM, Einevoll GT, and Ness TV (2021). Biophysically detailed forward modeling of the neural origin of EEG and MEG signals. Neuroimage 225, 117467. [PubMed: 33075556]

143. Sherman MA, Lee S, Law R, Haegens S, Thorn CA, Hämäläinen MS, Moore CI, and Jones SR (2016). Neural mechanisms of transient neocortical beta rhythms: Converging evidence from humans, computational modeling, monkeys, and mice. Proc. Natl. Acad. Sci. USA 113, E4885–E4894. [PubMed: 27469163]

144. Schroeder CE, Mehta AD, and Givre SJ (1998). A spatiotemporal profile of visual system activation revealed by current source density analysis in the awake macaque. Cerebr. Cortex 8, 575–592. 10.1093/cercor/8.7.575.

145. Lakatos P, Musacchia G, O'Connel MN, Falchier AY, Javitt DC, and Schroeder CE (2013). The spectrotemporal filter mechanism of auditory selective attention. Neuron 77, 750–761. [PubMed: 23439126]

146. Lakatos P, Barczak A, Neymotin SA, McGinnis T, Ross D, Javitt DC, and O'Connell MN (2016). Global dynamics of selective attention and its lapses in primary auditory cortex. Nat. Neurosci. 19, 1707–1717. 10.1038/nn.4386. [PubMed: 27618311]

Highlights

- Model of auditory thalamocortical circuits integrates multiscale experimental data
- Simulates physiological membrane voltages, firing rates, LFP/CSD, and EEG signals
- LFP/CSD oscillation events across frequencies match spontaneous *in vivo* data
- Predicts cellular and circuit mechanisms underlying LFP/CSD oscillation events

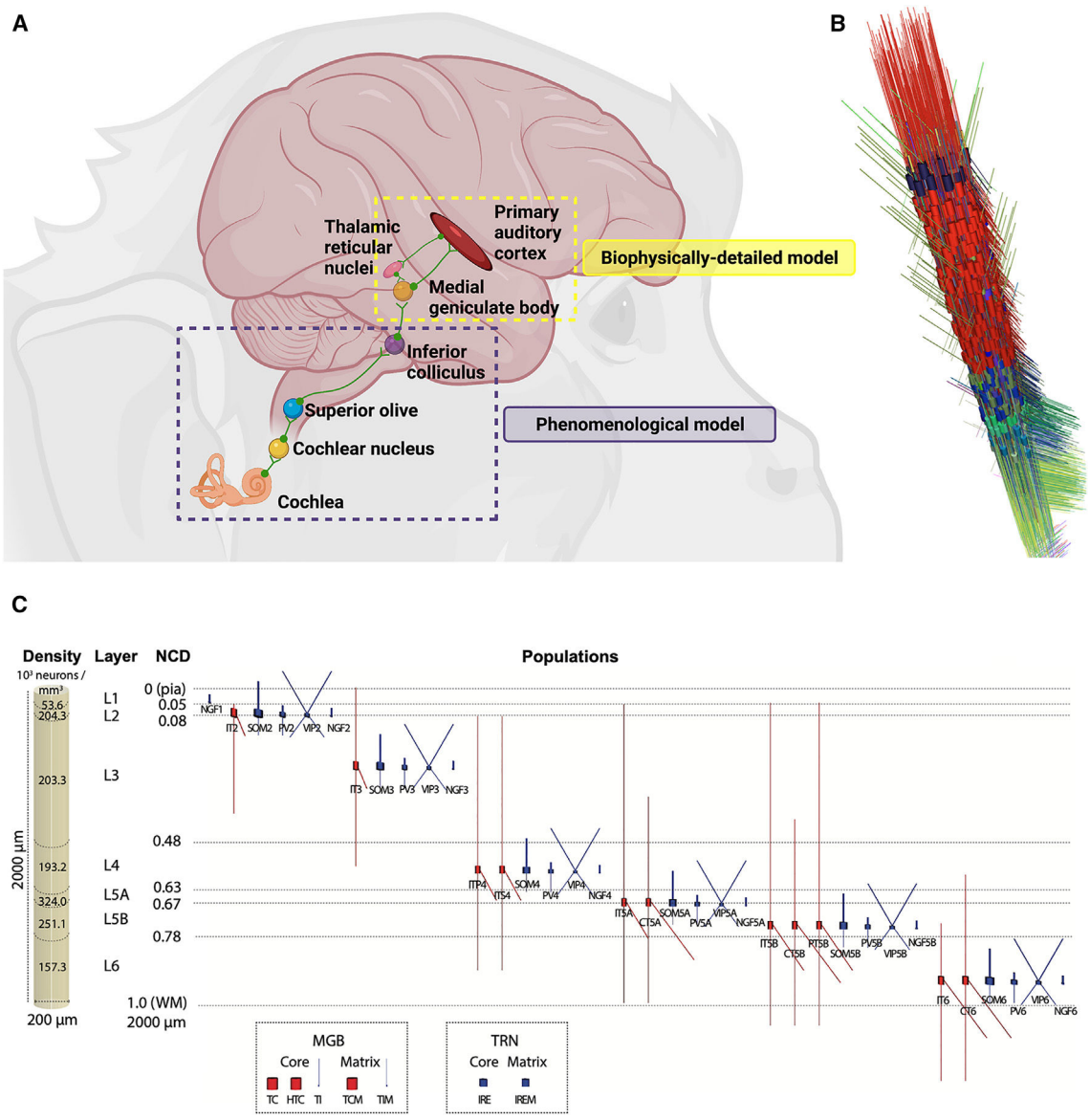

Figure 1. Overview of the macaque auditory system model and the biophysically detailed auditory thalamocortical circuits model

(A) A phenomenological model is used to capture the transformation of input sound into electrical impulses in the cochlea, superior olive, and inferior colliculus (IC). Output from IC then drives a detailed biophysical model of auditory thalamocortical circuits, including medial geniculate body (MGB), thalamic reticular nuclei (TRN), and primary auditory cortex (A1). Note that many of the connections are bidirectional but are not shown for simplicity.

(B) 3D representation of the A1 column model (only 20% of neurons are shown for clarity).

(C) Dimensions of simulated A1 column with laminar cell densities, layer boundaries, cell morphologies, and distribution of populations. Medial geniculate body (MGB) and thalamic reticular nuclei (TRN) populations' simplified morphologies are shown on the bottom, highlighting distinct core- and matrix-projecting populations. All models are conductance

based with multiple ionic channels tuned to reproduce the cell's electrophysiology. NCD denotes normalized cortical depth with values ranging from 0 (pia) to 1 (white matter [WM]).

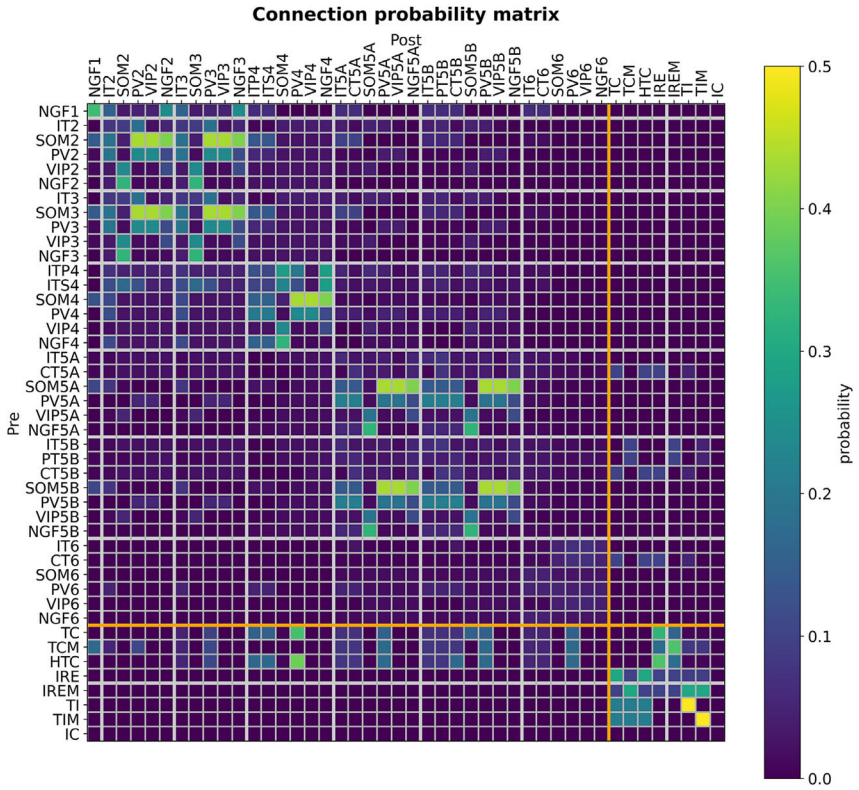

Figure 2. Connectivity matrix of model thalamocortical populations

Probability of connection between all 36 cortical and 6 thalamic populations. Horizontal and vertical thick white lines separate cortical layers, and thick orange lines separate cortex from thalamus. Note that the IC→MGB connection is not shown as there is no feedback connection from MGB→IC in our model, given that we use phenomenological cochlea/IC models (see STAR Methods).

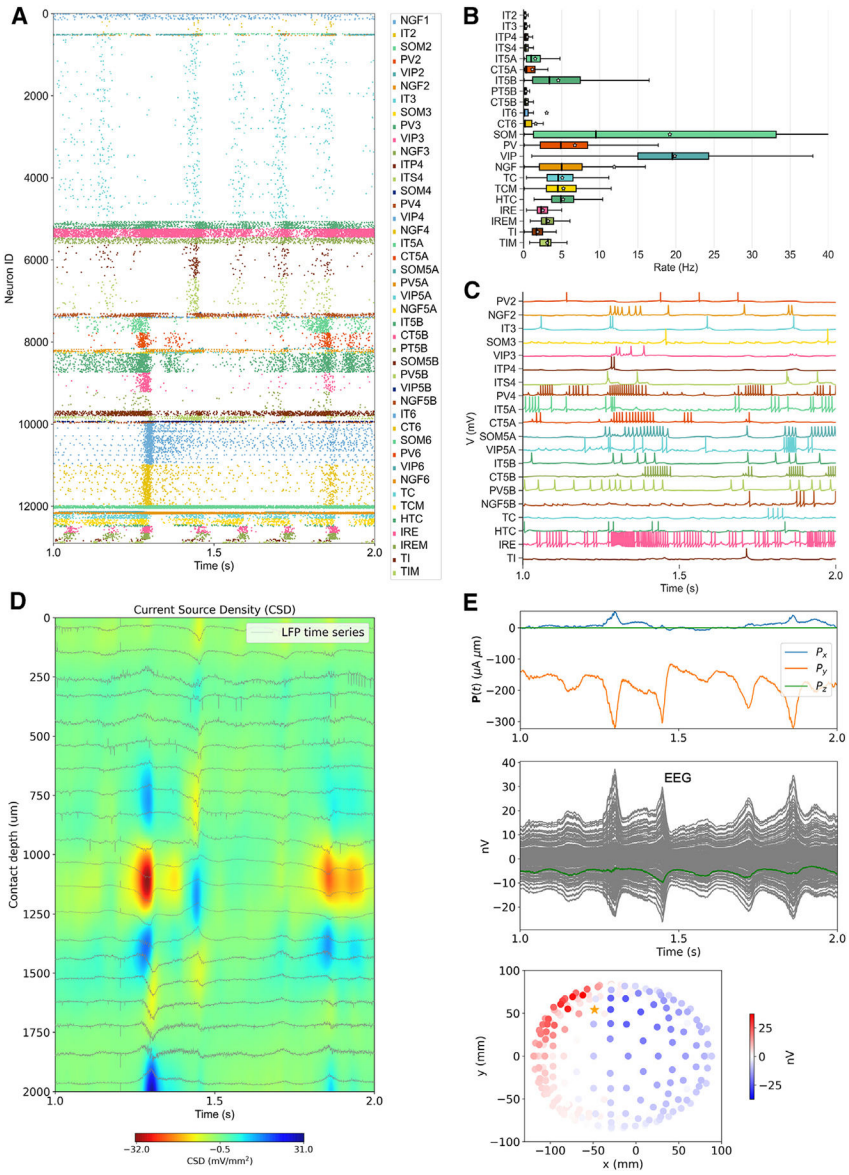

Figure 3. Cell-type- and layer-specific activity recorded at multiple scales

(A) Spiking raster plot.

(B) Box-and-whisker plot statistics of population firing rates (interneurons grouped across all layers) during simulation times from 1 to 11 s (box center and sides = mean and interquartile range [IQR]; whisker = 1.5 × IQR; stars = mean).

(C) Example voltage traces for different cell types and layers.

(D) Laminar CSD with LFP overlaid.

(E) Sum of current dipole moments across all neurons (top panel; Px, Py, and Pz indicate dipole moment orientations) used to calculate the EEG signals (middle and bottom panels) recorded from scalp electrodes distributed across a volume conduction head model (each electrode in gray; mean in green). All recordings arise from the same underlying biophysical model and are time-aligned starting at 1,000 ms of simulation time.

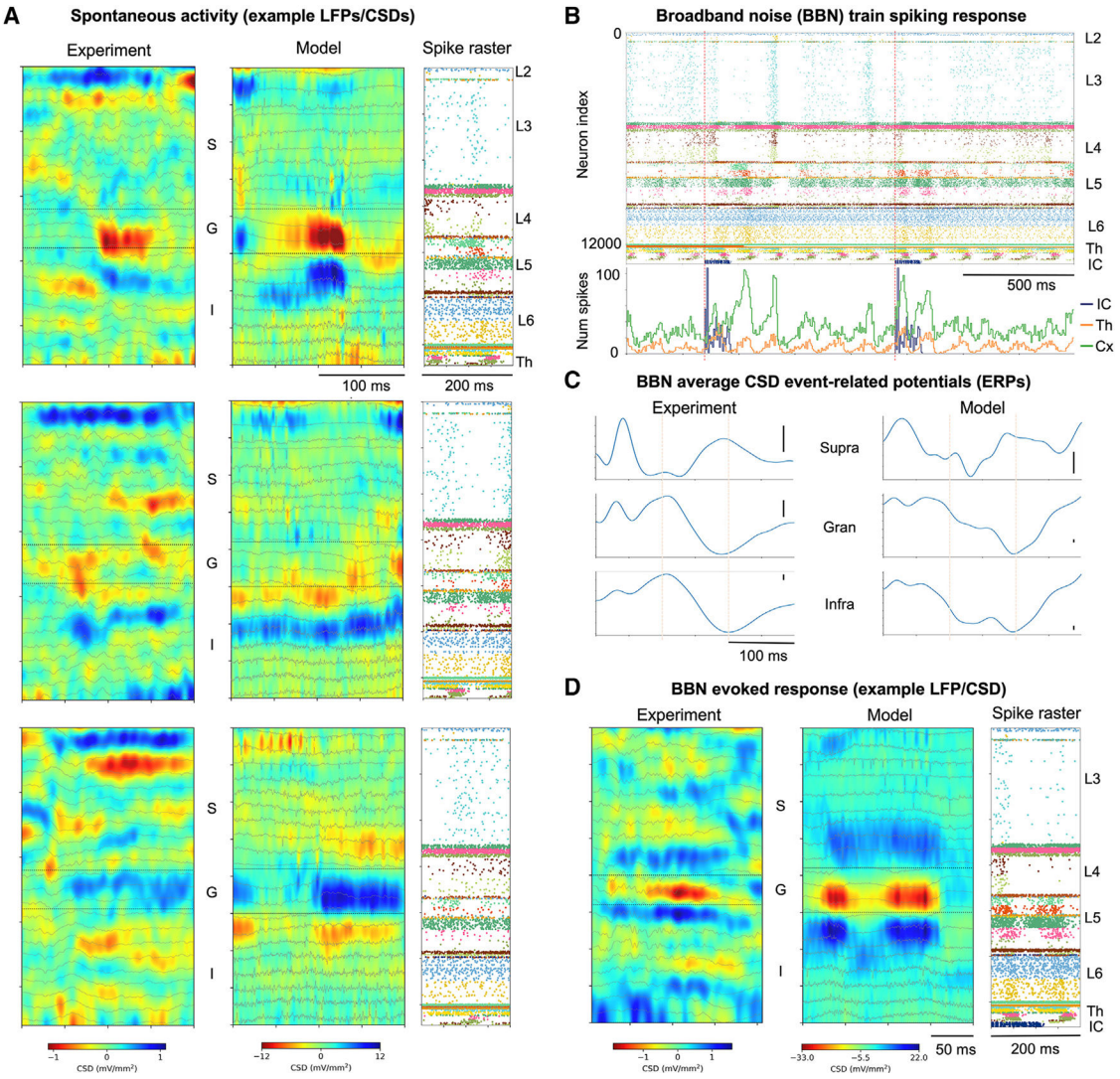

Figure 4. Example spiking and laminar LFP/CSD responses during spontaneous activity and broadband noise train stimuli and comparison to macaque *in vivo* LFP/CSD

(A) Comparison of example spontaneous LFP/CSD in model and macaque, illustrating the variability of spontaneous activity patterns and how the model reproduced some key features of each example pattern (e.g., in top-left example, a 50-ms-long current sink in the granular layer and current source in the infragranular layer). Transmembrane currents (sinks and sources) in CSD color maps are color coded red and blue, respectively. y axis represents LFP and related CSD channels at depths spanning pia to white matter, with supragranular (S), granular (G), and infragranular (I) layers indicated.

(B) Spiking raster plot and spike time histogram of the model's response to a broadband noise (BBN) stimulus train (red dotted line indicates BBN stimuli onset). (C) Comparison of macaque vs. model average CSD event-related potentials (ERPs) in response to BBN stimulus recorded at supragranular, granular, and infragranular layers (experiment, N = 122; model, N = 11; experiment scale bars represent 0.5 mV/mm^2; model scale bars represent 1 mV/mm^2; vertical dotted lines at 100 ms and 200 ms).

(D) Comparison of macaque and model example LFP/CSD response to BBN stimulus shows similar activation pattern (same color code and axes as in A).

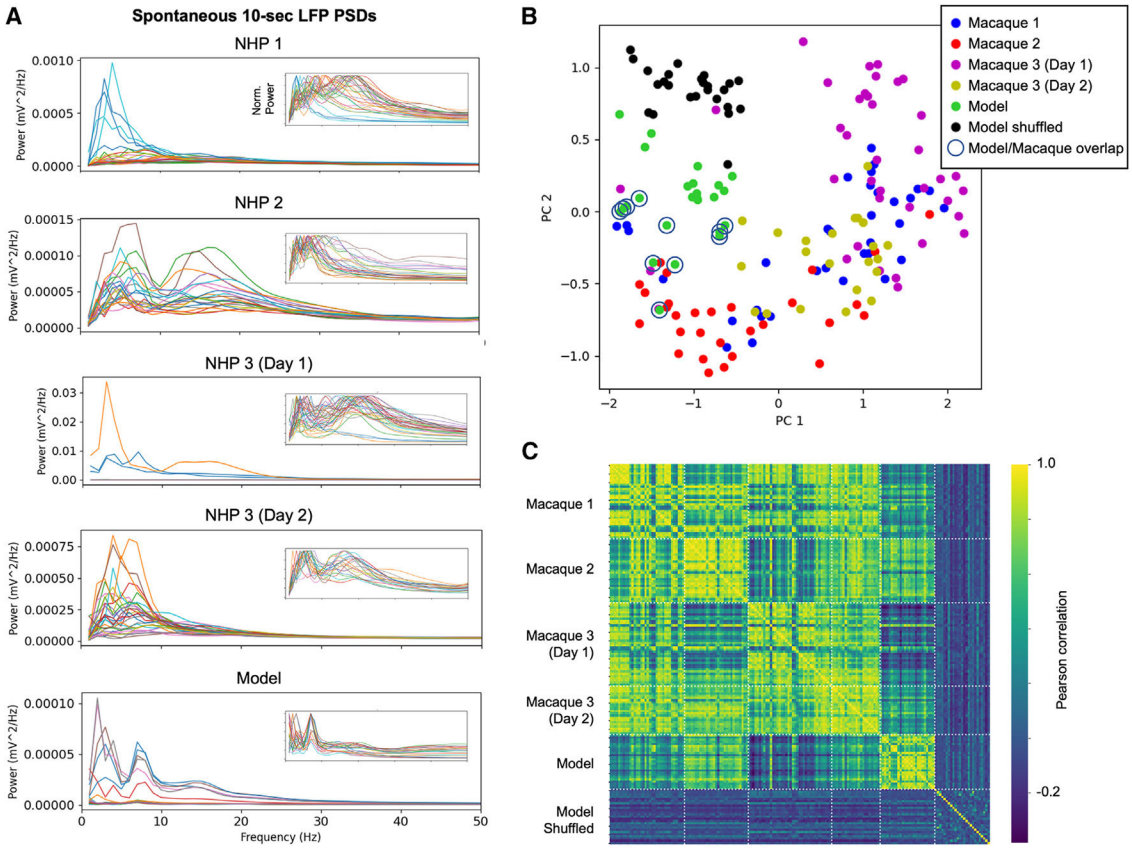

Figure 5. LFP PSD of macaques and model

(A) Power spectral densities (PSDs) of 10-s LFPs recorded from three macaques exhibit high variability within and across individuals and show features consistent with the model LFP PSD, including peaks at delta, theta/alpha, and beta. Insets show normalized PSDs.

(B) PCA of the LFP PSDs reveals an overlap between model and macaque that is absent in the shuffled model.

(C) Correlation matrix of LFP PSDs illustrates that the model is more strongly correlated with the macaques than the shuffled model.

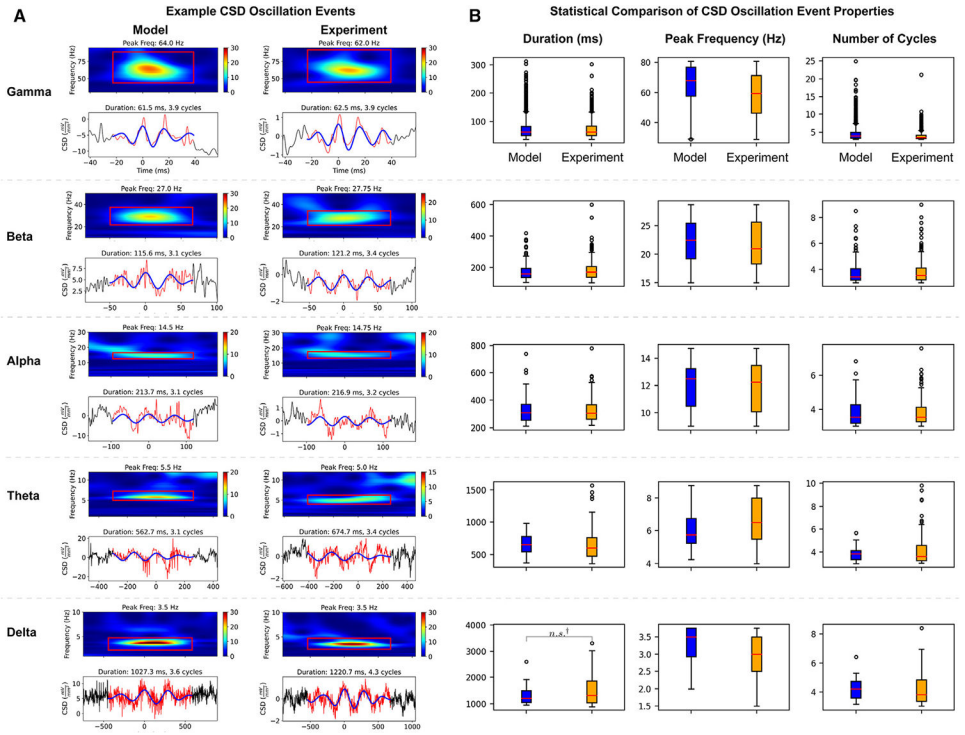

Figure 6. Comparison of spontaneous CSD oscillation events across frequency bands in the model and macaque experiments

(A) Examples of similar oscillation events detected across frequency bands in model (left) and macaque experiments (right). Each event is depicted with a CSD spectrogram (top panels; power units are $mV^2/mm^4/Hz$; red bounding box delineates the oscillation event) and the CSD time series signal (bottom panels; red: raw CSD time series, blue: bandpass-filtered CSD time series using cutoff frequencies shown in spectrogram red bounding box). Theta and alpha events are from supragranular layers, beta and delta from infragranular layers, and gamma from the granular layer.

(B) Statistical comparison of spontaneous CSD oscillation event properties in the model and macaque experiments. Oscillation events were detected in resting-state recordings, then sorted by frequency band: delta (N_{model} = 12; N_{exp} = 55), theta (N_{model} = 44; N_{exp} = 126), alpha (N_{model} = 59; N_{exp} = 138), beta (N_{model} = 192; N_{exp} = 318), and gamma (N_{model} = 2,359; N_{exp} = 1,625). The following oscillation event features were compared for each frequency band: duration (ms), peak frequency (Hz), and number of cycles. Box-and-whisker plots (box = interquartile range [IQR]; whisker = 1.5·IQR; orange line = median; black circles = outliers) compare the model and experimental data distributions for each feature and frequency band. Statistical analysis revealed no statistically significant differences between the model and experiment means (t test, $p > 0.05$, not significant, denoted by n.s.y; applies to all panels but only shown once for clarity).

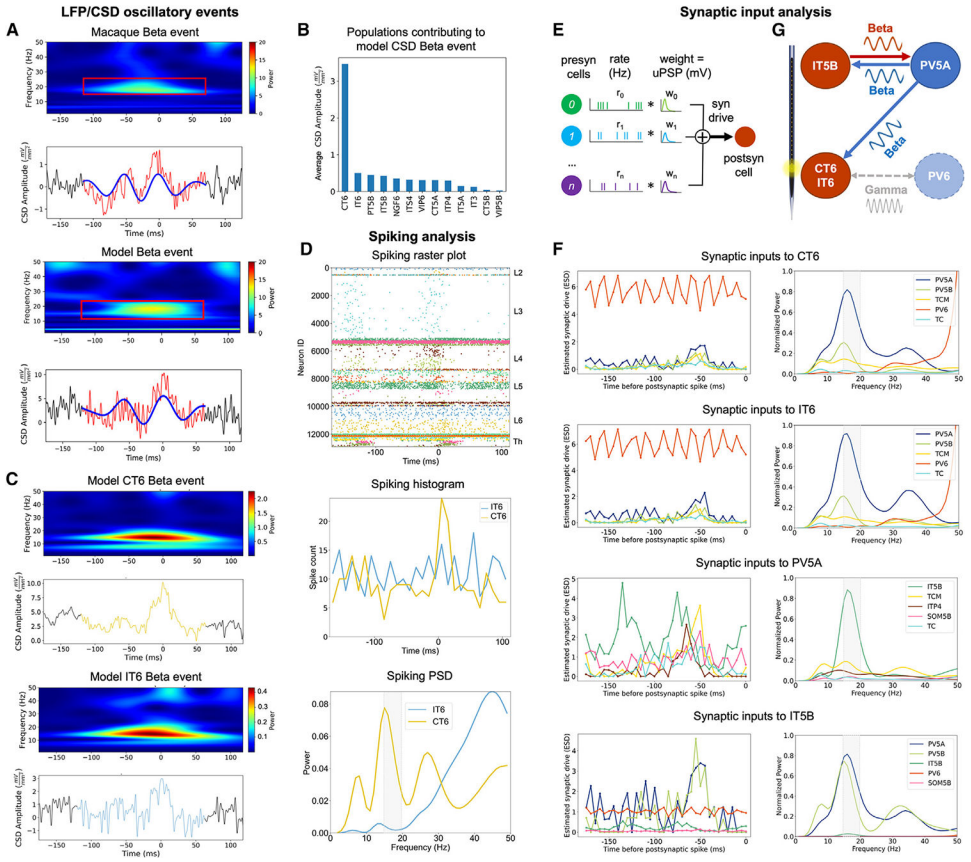

Figure 7. Model predicts layer- and cell-type-specific sources of LFP/CSD oscillatory events

(A) Similar CSD spontaneous beta oscillations were detected in macaque experiments (top) and model (bottom).

(B) Model populations with the strongest contribution to the CSD signal amplitude (mV/mm^2) during the time of the beta oscillation event at the corresponding electrode channel (depth 1,900 μm).

(C) CSD spectrogram and time series of the two populations (CT6 and IT6) with the strongest contributions to the beta oscillation event reveal consistent beta oscillatory events.

(D) Analysis of spiking activity (raster plot, histogram, and power spectral density) during the beta oscillation event reveals a similar spiking beta oscillatory pattern in CT6 but not IT6.

(E) Schematic of the method to estimate the synaptic input drive over time from different presynaptic populations based on the circuit spiking activity and connectivity.

(F) Analysis of synaptic input patterns to CT6, IT6, PV5A, and IT5B. Plots show time histogram and power spectral density (beta band highlighted in gray) of the estimated synaptic input patterns from the five strongest presynaptic populations targeting CT6, IT6, PV5A, and IT5B.

(G) Summary schematic of model prediction: the CSD beta event is generated by CT6/IT6 synaptic inputs originating in PV5A, which in turn result from beta oscillatory interactions between PV5A and IT5B.

KEY RESOURCES TABLE

REAGENT or RESOURCE	SOURCE	IDENTIFIER
Deposited data		
In Vivo Experimental data	Neymotin et al.[61]	Zenodo: https://doi.org/10.5281/zenodo.10066993
Data used to constrain the auditory thalamocortical model	This paper	Zenodo: https://doi.org/10.5281/zenodo.10066993
Auditory thalamocortical model output simulated data	This paper	Zenodo: https://doi.org/10.5281/zenodo.10066993
Software and algorithms		
Auditory thalamocortical model and data analysis source code	This paper; https://github.com/NathanKlineInstitute/Macaque_auditory_thalamocortical_model_data	N/A
NetPyNE	http://netpyne.org	Zenodo: https://doi.org/10.5281/zenodo.4767870
NEURON	https://neuron.yale.edu/	N/A
OEvent	https://github.com/NathanKlineInstitute/OEvent	N/A
UR EAR	https://www.urmc.rochester.edu/MediaLibraries/URMCMedia/labs/carney-lab/codes/UR_EAR_v2_1.zip	N/A
LFPykit	https://github.com/LFPy/LFPykit	Zenodo: https://doi.org/10.5281/zenodo.7820713
Python	http://python.org	N/A